Front page

Exam information
NFYK10020E - Physics Thesis 60 ECTS, Niels Bohr Institute - Contract:147474 (Yi Zhou)

Handed in by
Yi Zhou
hbq308@alumni.ku.dk

Exam administrators
Eksamen Nørre
eksamen-noerre@adm.ku.dk

Assessors
Vitor Cardoso
Examiner
vitor.cardoso@nbi.ku.dk
+4535323769

Marta Orselli
Co-examiner
orselli@nbi.ku.dk

Hand-in information

Title: Quasinormal Mode Instability: A Case Study in Schwarzschild-de Sitter Spacetime
Title, english: Quasinormal Mode Instability: A Case Study in Schwarzschild-de Sitter Spacetime
The sworn statement: Yes
Does the hand-in contain confidential material: No
Did you remember to fill out the AI declaration, which you should upload as an attachment?: Yes

UNIVERSITY OF COPENHAGEN
NIELS BOHR INSTITUTE

Master of Science in Physics

Yi Zhou

Quasinormal Mode Instability

A Case Study in Schwarzschild-de Sitter Spacetime

Date: May 2025

Advisor: Vitor Cardoso, Rodrigo Panosso Macedo

Abstract

The spectral instability of Quasinormal mode (QNM) is an interesting phenomenon in black hole (BH) physics and gravitational wave (GW) physics. Despite the dynamic stability of black hole spacetimes under perturbations, the spectra of perturbations in the form of the QNMs exhibit drastic changes under a minor perturbation of the background spacetime. We employ the hyperboloidal framework and the Analytical Mesh Refinement (AnMR) technique to control the geometry of spacetimes in a systematic and robust way, and to ensure enough numerical capability of solving the QNM problem under different geometrical limits of SdS spacetime. We are able to learn the behaviors of QNM spectra under different background perturbations. In short, when a small cosmological constant perturbs the Schwarzschild spacetime, the branch cut structure in its QNM spectrum gets destroyed and purely imaginary de Sitter modes emerges from $r_H\omega = 0$, which is interpreted as a manifestation of QNM instability.

Table of content

1 Introduction

Black hole perturbation theory provides us with a well-established probe of black hole spacetimes, as it can extract the key feature quasinormal modes from gravitational waves outside of the black hole, where the feature is determined only by the black hole spacetime itself and independent of the perturbative source. The method is extensively employed in analyzing real world observational data of GW signals from astronomical events like binary compact object mergers [1, 2, 3, 4], and has the potential to probe the mass, charge, angular momentum of the black hole as well as the cosmological constant of the background.

When accessed at a fixed spatial position, the time evolution of the GWs of scalar field perturbations usually show three distinct phases, the initial prompt phase, the ringdown phase characterized by the QNMs, and the late time tail phase. The predicted ringdown phase by calculations of perturbative method, as a superposition of exponentially decaying QNM wave forms, has seen a good success agreeing with observational data in refs. [1, 5, 6]. With a Fourier transformation, the ringdown phase GW wave form could be decomposed into a set of discrete quasinormal modes, which has been proved with dynamical stability in many different scenarios in refs. [7, 8, 9, 10].

The Schwarzschild-de Sitter (SdS) spacetime describes a non-spinning, non-charged black hole living on the background of a de Sitter spacetime. It is found by combining the metrics of the Schwarzschild spacetime and the de Sitter spacetime. Geometrically the regime of SdS spacetime could be entered by deforming the Schwarzschild spacetime with a small parameter $\sqrt{\Lambda}$ or equivalently with the inverse of cosmological horizon $1/r_\Lambda$. The other approach is to deform the de Sitter spacetime with a small parameter M or equivalently with the black hole horizon r_H. Speaking of the quasinormal modes associated with the spacetime, the Schwarzschild spacetime has a set of complex modes associated with the spacetime light ring [7, 8, 9, 10], as well as a branch cut along the imaginary axis emerging from $\omega = 0$ [7]. The dS spacetime only shows a discrete set of modes along the imaginary axis [11, 12, 13]. The SdS spacetime combines the two sets of discrete modes, and this thesis aims at studying the emergence of these two families from the perspective of QNM instability.

The study of the aforementioned QNMs in SdS spacetime implies real world application since cosmological observations assume a positive cosmological constant, or an asymptotically de Sitter spacetime for our universe. All black holes live with a small but non-zero cosmological constant in a cosmological scale, whose GWs should be therefore affected. There is current interest in the late time tail decay of gravitational waves in refs. [14, 15, 16, 17], which studies the effect on GW tails from a positive cosmological constant. In [18] a significant change in the behavior of the late time tail is found with even a small cosmological constant added compared to Schwarzschild spacetime.

There has been numerous studies on the behaviors of QNM families for black hole spacetimes with more than one parameter. Ref. [13] identified 3 families of QNMs in the Reisnners-Nördstrom-de Sitter spacetime, one family directly related to the light ring modes associated with the presence of the black hole horizon, a second family of purely imaginary modes related to the new time scales introduced by the de Sitter horizon, and also a third family of QNMs resulting from the electric charge of Reisnners-Nördstrom black hole. Here only the first two families are relevant in our scenario: the light ring modes and the de Sitter modes. Refs. [19, 20, 21] elaborately introduced a geometrical framework to deal with the perturbations on Kerr-de Sitter spacetime, and proved the stability of such spacetime in the sense that asymptotically Kerr-de Sitter spacetimes must decay to an exact Kerr-de Sitter solution. The papers also introduced a general scheme to find out the parameters of the exponentially decaying tails of GWs on perturbed Kerr-de Sitter family of black hole spacetimes.

The boundary conditions has always been a delicate issue for solving the QNM eigenfunctions in black hole perturbation theory, because within the formulation with Schwarzschild-like coordinates, the eigenfunctions diverge to infinity near the BH and cosmological horizon. Ref. [22] performed a systematic study of these QNM families, where the authors employed a spectral method numerical technique based on the so-called Bernstein polynomials. The usefulness of these non-orthogonal basis functions was highlighted in numerical studies [23] with focus on their capability of handling boundary conditions in ordinary differential eigenvalue problems.

Recently, the hyperboloidal framework has emerged as robust geometrical approach to study QNMs in BH pertubation theory allowing us to overcome the ill-representation of the QNM eigenfunctions at the horizons. In the framework, the treatment of the boundary conditions is accomplished by an appropriate spacetime parameterization in terms of hyperboloidal time surfaces, with a compact radial coordinate defined thereon. The appropriate coordinates allow the QNM eigenfunctions to become regular at the horizons [24, 25, 26], see sec. 4. Recently refs. [27, 28] employed the hyperboloidal approach and pseudospectrum analysis to investigate the spectral instability of QNMs under external perturbations for asymptotically flat spacetimes and asymptotically de Sitter spacetimes. Following the interpretation on QNM instability put forward in ref. [27, 28, 29], this thesis focuses on the perturbation on the background spacetime, specifically the de Sitter parameter as a perturbation on Schwarzschild spacetime, or vice-versa, the Schwarzschild parameter as a perturbation on de Sitter spacetime.

In this thesis we will show that the choice of radial compactification offers us a freedom to parametrically study all limits of the spacetime within a robust framework akin to the rigorous geometrical approach put forward by Geroch [30]. With the geometrical aspects under our control, we employ numerical techniques from spectral methods based on standard orthogonal basis functions (such as the Chebyshev polynomials), without having to employing more intricate non-orthogonal basis as suggested in ref. [23]. In particular, this thesis performs a comprehensive study of the so-called Analytical Mesh Refinement technique in the context of QNM. While this technique had been employed in different contexts [31, 32, 33], a systematic study of its applicability in the QNM context was missing. The QNM problem in SdS spacetime offers a well-defined setup for such studies, see sec. 6. In the context of perturbation theory, the AnMR shows distinct advantages over the traditional approach in the self-force program as it allowed to accurately resolve the solution of particles orbiting a black hole with extremely large orbital radii or having angular modes with very high spherical harmonic mode index [33]. On the technical side, our work finds that the utilization of AnMR helps improve numerical capabilities in the QNM problem, especially for numerically difficult situations such as QNMs with high overtone indexes.

The hyperboloidal framework provides a clean setup to study the spacetime limits of the Schwarzschild-de Sitter spacetime. One important finding of this thesis is the interpretation of the behaviors of QNMs in the Schwarzschild limit. Compared to the branch cut that arises in Schwarzschild spacetime, SdS spacetime has a clean discrete set of QNM frequencies. Therefore the setup allows us to delve on this issue. We find that with the perturbation of the cosmological constant, the light ring modes deform smoothly, while the de Sitter modes along the imaginary axis emerge and destroy the branch cut. Under the limit of $\Lambda \to 0$, the de Sitter modes accumulate at $\omega = 0$ which corresponds to the branch cut structure in the limit to Schwarzschild spacetime.

2 Schwarzschild-de Sitter spacetime

The Schwarzschild spacetime is a spherically symmetric solution of the vacuum Einstein field equations with a vanishing cosmological constant. It describes a non-spinning, non-charged black hole spacetime that is asymptotically flat if measured from far away. The de Sitter spacetime is a maximally symmetric solution of the vacuum Einstein field equations with a positive cosmological constant. It is the simplest spacetime with a constant positive curvature.

The Schwarzschild-de Sitter spacetime could be interpreted as a natural combination of the two spacetimes, where the spherically symmetric black hole lives on a background spacetime with a positive constant curvature rather than a flat background. The spacetime has two horizons, the black hole horizon and the cosmological horizon. A typical observer, who hasn't fallen into the black hole while still could see the black hole, lives between the two horizons. Given current cosmological observations that are supporting a positive cosmological constant, the Schwarzschild-de Sitter spacetime could model simple black holes living on our Universe that is asymptotically de Sitter.

2.1 Derivation of Schwarzschild-de Sitter metric

The Schwarzschild-de Sitter spacetime features a static and spherically symmetric metric with a positive constant scalar curvature. In Schwarzschild-like coordinates (t, r, θ, φ), the line element of the SdS spacetime reads in its most common form

$$\begin{aligned} ds^2 &= -f(r)dt^2 + f^{-1}(r)dr^2 + r^2 d\varpi^2, && (1) \\ f(r) &= 1 - \frac{2a}{r} - br^2 && (2) \end{aligned}$$

with $d\varpi^2 = d\theta^2 + \sin^2\theta d\varphi^2$ the line element of the 2-sphere. The two parameters inside the function $f(r)$, which characterizes the geometry of the spacetime, have physical implications through the following relation with the black hole mass M and the cosmological constant Λ,

$$a = M, \quad b = \frac{\Lambda}{3}. \tag{3}$$

Under the limitations of either of the above two parameters vanishes, the line element will be reduced to that of the de Sitter metric or the Schwarzschild metric.

In a similar manner with the Birkhoff's theorem of the Schwarzschild spacetime, we can prove that any spherically symmetric metric that solves the Einstein field equations with a positive cosmological constant could be written in the form of eq. (1).

A metric that is spherically symmetric, *i.e.* invariant under rotations, can be dependent only on $d\varpi^2 = d\theta^2 + \sin^2\theta d\varphi^2$ with respect to the angular coordinates θ and φ if written in spherical coordinates (t, r, θ, φ). That is, in another way, the most generic form of such a metric will read,

$$ds^2 = -A(t,r)dt^2 + 2B(t,r)dtdr + C(t,r)dr^2 + D(t,r)d\varpi^2. \tag{4}$$

We assume the function $D(t, r)$ cannot be constant on any 3-dimensional space-like submanifold of the whole spacetime, which would correspond to a spacetime with a constant radius. This assumption could be derived directly from the asymptotic behavior of the spacetime metric that we would like to see, in this case asymptotically de Sitter. However in extremal cases it does not hold, *e.g.* the Nariai spacetime discussed in sec. 5.3. On the aforementioned assumption we could define a set of new coordinates

$$t'(t,r) = t, \quad r'(t,r) = \sqrt{D(t,r)}. \tag{5}$$

Then the line element will read

$$ds^2 = -A'(t',r')dt'^2 + 2B'(t',r')dt'dr' + C'(t',r')dr'^2 + r'^2 d\varpi^2. \tag{6}$$

To eliminate the cross term in the line element, we could find the coordinate transformation by leaving the spatial coordinate unchanged and integrating to get the time coordinate through

$$dt'' = E(t', r') \Big[A'(t', r')dt' - B'(t', r')dr'\Big], \tag{7}$$

where the function $E(t', r')$ is determined by the relation $\frac{\partial}{\partial r'}\left(\frac{\partial t''}{\partial t'}\right) = \frac{\partial}{\partial t'}\left(\frac{\partial t''}{\partial r'}\right)$ to make a closed differential form. Therefore the most generic line element eq. (4) could then be written in a form of

$$ds^2 = -e^{2\alpha(t,r)}dt^2 + e^{2\beta(t,r)}dr^2 + r^2 d\varpi^2, \tag{8}$$

where we are left with two undetermined functions $\alpha(t, r)$ and $\beta(t, r)$ in the metric.

To derive the Schwarzschild-de Sitter metric as the form in eq. (1), we need to impose on it the restrictions coming from the Einstein field equations with a non-zero cosmological constant

$$R_{\mu\nu} - \frac{1}{2}Rg_{\mu\nu} + \Lambda g_{\mu\nu} = 8\pi T_{\mu\nu}. \tag{9}$$

Since the stress-energy tensor $T_{\mu\nu}$ vanishes for a vacuum solution, we could get the restrictions on $R_{\mu\nu}$ by contracting eq. (9) with the metric $g^{\mu\nu}$, which leads to

$$R = 4\Lambda, \quad R_{\mu\nu} = \Lambda g_{\mu\nu}. \tag{10}$$

With the line element eq. (8), we can compute the Ricci tensor as following listed

$$\begin{aligned}
R_{tt} &= e^{2\alpha-2\beta}\left\{\partial_r^2\alpha - \partial_r\alpha\partial_r\beta + (\partial_r\alpha)^2 + \frac{2}{r}\partial_r\alpha\right\} + \left\{\partial_t^2\beta - \partial_t\alpha\partial_t\beta + (\partial_t\beta)^2\right\}, && (11)\\
R_{rr} &= -\left\{\partial_r^2\alpha - \partial_r\alpha\partial_r\beta + (\partial_r\alpha)^2 - \frac{2}{r}\partial_r\beta\right\} + e^{-2\alpha+2\beta}\left\{\partial_t^2\beta - \partial_t\alpha\partial_t\beta + (\partial_t\beta)^2\right\}, && (12)\\
R_{tr} &= \frac{2}{r}\partial_t\beta, && (13)\\
R_{\theta\theta} &= 1 + e^{-2\beta}\Big[r(\partial_r\beta - \partial_r\alpha) - 1\Big], && (14)\\
R_{\varphi\varphi} &= \sin^2\theta\left\{1 + e^{-2\beta}\Big[r(\partial_r\beta - \partial_r\alpha) - 1\Big]\right\}, && (15)
\end{aligned}$$

and the scalar curvature as well

$$R = -2e^{-2\beta}\left[\partial_r^2\alpha - \partial_r\alpha\partial_r\beta + (\partial_r\alpha)^2 + \frac{2}{r}(\partial_r\alpha - \partial_r\beta) + \frac{1}{r^2}(1 - e^{2\beta})\right]. \tag{16}$$

First of all, the restriction $R_{tr} = 0$ leads directly to the function β being dependent only on the spatial coordinate

$$\partial_t\beta = 0, \quad \beta(t, r) = \beta(r). \tag{17}$$

Then if we take the partial derivative with respect to time t on the equation $R_{\theta\theta} = \Lambda g_{\theta\theta} = \Lambda r^2$, we immediately get

$$\partial_t\partial_r\alpha = 0, \quad \alpha(t, r) = \alpha_t(t) + \alpha_r(r). \tag{18}$$

Combining the conditions in eqs. (17) and (18), we find that the line element eq. (8) could be further simplified through defining a new time coordinate $\tilde{t}$ with $d\tilde{t} = \alpha_t(t)dt$. Or in another way, we are therefore able to find a time coordinate $\tilde{t}$ for which $\tilde{\alpha}(\tilde{t}, r) = \alpha_r(r)$. Now that we have proven that the line element of eq. (4) can always be expressed in a static form, *i.e.* a form not dependent on the time coordinate, in the following discussions we will use the static line element as a starting point. We could then find the exact forms of the functions $\alpha(r)$ and $\beta(r)$ by imposing the rest of the restrictions from the Einstein field equations.

We could notice that according to eq. (10), each of R_{tt} and R_{rr} doesn't vanish individually, but a combination of both vanishes just like the case in the Birkhoff's theorem of the Schwarzschild spacetime.

$$0 = \left(e^{-2\alpha+2\beta} g_{tt} + g_{rr}\right) \Lambda = e^{-2\alpha+2\beta} R_{tt} + R_{rr} = \frac{2}{r}(\partial_r \alpha + \partial_r \beta). \tag{19}$$

This will require the sum of the two functions $\alpha(r) + \beta(r)$ to be a constant. Such a constant could be eliminated by changing the time coordinate $t \to t' = e^c t$, where c is a specific constant chosen to vanish the sum of $\alpha(r) + \beta(r)$. Therefore, we could safely impose

$$\alpha(r) = -\beta(r). \tag{20}$$

We only need to set the following to obtain a generic line element eq. (1) for spherically symmetric spacetimes.

$$\alpha(r) = \frac{1}{2} \ln f(r). \tag{21}$$

Both the restrictions on $R_{\theta\theta}$ and $R_{\varphi\varphi}$ requires the same thing, which reads with eq. (20)

$$e^{2\alpha} \left(2r\partial_r \alpha + 1\right) = 1 - \Lambda r^2. \tag{22}$$

Noting that the LHS of the above equation equals $\partial_r(re^{2\alpha})$, the equation finally solves with

$$e^{2\alpha} = 1 - \frac{r_0}{r} - \frac{\Lambda}{3} r^2, \tag{23}$$

where r_0 is the constant of integration that we recognize as the Schwarzschild radius under the trivial condition of a zero cosmological constant. It is easy to check the rest of conditions eq. (11) is also satisfied (in fact it is equivalent to taking the derivative of eq. (22)). Therefore, we have finally derived the line element eq. (1) as a solution of the Einstein field equations with a non-zero cosmological constant.

2.2 Geometry of the Schwarzschild-de Sitter spacetime

As an alternative way of describing the the function $f(r)$ in eq. (1), we could instead use the two real and positive roots of $f(r)$, which helps us to track the geometry of the spacetime more conveniently in most cases. Specifically, the metric function reads

$$\begin{aligned} f(r) &= 1 - \frac{2M}{r} - \frac{\Lambda}{3} r^2 \\ &= -\frac{\Lambda}{3} r^2 \left(1 - \frac{r_H}{r}\right)\left(1 - \frac{r_\Lambda}{r}\right)\left(1 - \frac{r_o}{r}\right). \end{aligned} \tag{24}$$

with the two positive roots $r_\Lambda \geq r_H \geq 0$ representing the cosmological horizon and the black hole horizon respectively, and $r_o = -(r_H + r_\Lambda)$ the third and negative root of $f(r)$. It is also convenient to define the tortoise coordinate $r_*(r)$ via $dr_*/dr = 1/f(r)$, which integrates to

$$\begin{aligned} r_* \;&=\; \frac{3r_H}{\Lambda(r_\Lambda - r_H)(r_H - r_o)} \ln\left|1 - \frac{r_H}{r}\right| \\ &+\; \frac{3r_\Lambda}{\Lambda(r_H - r_\Lambda)(r_\Lambda - r_o)} \ln\left|1 - \frac{r_\Lambda}{r}\right| \\ &+\; \frac{3r_\Lambda}{\Lambda(r_H - r_o)(r_o - r_\Lambda)} \ln\left|1 - \frac{r_o}{r}\right|. \end{aligned} \tag{25}$$

By comparing the coefficients of each term in eq. (24), one directly derives the relation between the parameters Λ and M and the horizons via

$$\Lambda = \frac{3}{r_H^2 + r_H r_\Lambda + r_\Lambda^2}, \tag{26}$$

$$M = \frac{r_H r_\Lambda \left(r_H + r_\Lambda\right)}{2\left(r_H^2 + r_H r_\Lambda + r_\Lambda^2\right)}. \tag{27}$$

Alternatively, Cardano's formular for a cubic equation gives for $\phi = \arccos(3M\sqrt{\Lambda})$

$$r_H = \frac{1}{\sqrt{\Lambda}}\left(\cos\left(\frac{\phi}{3}\right) - \sqrt{3}\sin\left(\frac{\phi}{3}\right)\right), \tag{28}$$

$$r_\Lambda = \frac{1}{\sqrt{\Lambda}}\left(\cos\left(\frac{\phi}{3}\right) + \sqrt{3}\sin\left(\frac{\phi}{3}\right)\right). \tag{29}$$

It is evident that the horizons' coordinate location changes with respect to the parameters M and Λ, i.e., $r_h(M,\Lambda)$ and $r_\Lambda(M,\Lambda)$. As expected, eqs. (28) and (29) yields

$$\lim_{\Lambda\to 0^+} r_H(M,\Lambda) = 2M, \ \lim_{\Lambda\to 0^+} r_\Lambda(M,\Lambda) = +\infty, \tag{30}$$

$$\lim_{M\to 0} r_H(M,\Lambda) = 0, \ \lim_{M\to 0} r_\Lambda(M,\Lambda) = \sqrt{\frac{3}{\Lambda}}, \tag{31}$$

which corresponds to the respective limits to Schwarzschild spacetime and de Sitter spacetime.

From the two characteristic length scales provided by the horizons, in this work we introduce a description of SdS geometry by an one-parameter family of solution via the dimensionless variable

$$\eta = \frac{r_H}{r_\Lambda}. \tag{32}$$

Even though $\eta \in [0,1]$, there are actually three different limits of the spacetime to be considered for a geometrical completeness. The limit $\eta \to 0$ corresponds either to the Schwarzschild limit via eqs. (30) or de Sitter limit via eqs. (31). Moreover, the Nariai solution arises in the extremal limit $\eta \to 1$ if we choose the typical length scales to study the near horizon regions. Under such limit, the black hole singularity goes to infinity and the surface areas of both horizons are the same.

3 Black Hole Perturbation Theory

Given the metric of the SdS spacetime, we would like to investigate the perturbations of such spacetime to study the stability of the gravitational system and analyze the gravitational waves that propagate through the spacetime. Such analysis is performed within the framework of linearized gravitational perturbations of spherically symmetric black hole spacetimes [9] and analysis tools of the quasinormal modes (QNMs).

In a general form, we are trying to address a spacetime with the metric $g_{\mu\nu}$ and matter fields cumulatively noted as Φ. The Einstein-Hilbert action of such system reads

$$S = \int d^4x\sqrt{-g}\left\{\frac{1}{16\pi}(R - 2\Lambda) + \mathcal{L}_M\right\}, \tag{33}$$

where $\mathcal{L}_M$ represents the Lagrangian associated with all matter fields at present. The equations of motion associated with the action eq. (33) are the Einstein field equations eq. (9) and the corresponding equations of motion for all the matter fields with a possible coupling with spacetime curvature.

For perturbations on the background spacetime, we can write the fields as

$$g_{\mu\nu} = g^{BG}_{\mu\nu} + h_{\mu\nu}, \quad \Phi = \Phi^{BG} + \Psi, \tag{34}$$

where the superscript "BG" represents the fields of the background spacetime. Assuming small enough perturbations, we can linearize the system with respect to the perturbation fields $h_{\mu\nu}$ and Ψ to get the equations of motion for these fields.

In this work we will focus on the study case of scalar field perturbations, whose Lagrangian reads

$$\mathcal{L}_{\text{scalar}} = -(\partial_\mu \Phi)^\dagger \, \partial^\mu \Phi - \xi R \, \Phi^\dagger \Phi - m^2 \, \Phi^\dagger \Phi, \tag{35}$$

where ξ is the curvature coupling constant and m is the mass of the scalar field. The equations of motion for the scalar field read

$$\left(\nabla_\mu \nabla^\mu - \xi R - m^2\right) \Phi = 0, \tag{36}$$

and together with the Einstein field equations eq. (9) form a full set of equations of motion for such a system. With the perturbations $g_{\mu\nu} = g^{BG}_{\mu\nu} + h_{\mu\nu}$ and $\Phi = \Phi^{BG} + \Psi$ where $\Phi^{BG} = 0$, we find that the background g^{BG} simply needs to satisfy the vacuum Einstein field equations

$$R^{BG}_{\mu\nu} - \frac{1}{2} R^{BG} g^{BG}_{\mu\nu} + \Lambda g^{BG}_{\mu\nu} = 0, \tag{37}$$

while the linearized equations of motion for $h_{\mu\nu}$ and Ψ decouple. Assuming a massless scalar field $m = 0$ and a vanishing curvature coupling $\xi = 0$, the equation of motion for the scalar field will read

$$\frac{1}{\sqrt{-g_{BG}}} \partial_\mu \left(\sqrt{-g_{BG}} \, g^{\mu\nu}_{BG} \, \partial_\nu \Psi\right) = 0. \tag{38}$$

For a background of spherically symmetric black hole spacetime, the second order partial derivative equation eq. (38) in terms of (t, r, θ, φ) could be separated with a decomposition with spherical harmonics and a Fourier transformation on the time coordinate t

$$\Psi(t, r, \theta, \varphi) = \sum_{\ell, m} \frac{\Psi_{\ell m}(t, r)}{r} Y_{\ell m}(\theta, \varphi), \tag{39}$$

$$\Psi_{\ell m}(t, r) = \int d\omega \, e^{-i\omega t} \psi_{\ell m\omega}(r). \tag{40}$$

Therefore, by plugging eq. (39) into eq. (38) in our case of a spherically symmetric spacetime eq. (1), it will lead to the Schrödinger-like equation

$$\frac{d^2}{dr_*^2} \psi_{\ell m\omega} - \left(V_\ell - \omega^2\right) \psi_{\ell m\omega} = 0, \tag{41}$$

with the effective potential

$$V_\ell(r) = f(r) \left(\frac{\ell(\ell+1)}{r^2} + \frac{f'(r)}{r}\right). \tag{42}$$

3.1 Quasinormal modes

Quasinormal modes of black holes are eigensolutions of eq. (41) which satisfy certain boundary conditions at the black hole event horizon ($r_* \to -\infty$) and the asymptotic region ($r_* \to +\infty$) [9, 8, 7]. The latter boundary can be varying for different cases, for example at spatial infinity for asymptotically flat spacetimes or at the cosmological horizon in our case of SdS spacetime. General quasinormal modes describe a perturbed system with a dissipating total energy. For perturbations of black hole spacetimes, that will correspond to ingoing waves at the black hole horizon and outgoing waves in the asymptotic region.

Since the effective potential vanishes at both horizons ($r_* \to \pm\infty$) according to eq. (42) in SdS spacetime, the solutions of eq. (41) approximate to

$$\psi_{\ell m\omega}(r) \sim e^{\pm i\omega r_*} \quad \text{or} \quad \Psi_{\ell m}(t,r) \sim e^{-i\omega(t\mp r_*)}. \tag{43}$$

Combining this with the physical condition of the direction of energy flows, we will get

$$\begin{aligned} \psi_{\ell m\omega}(r) &\sim e^{+i\omega r_*}\,, \quad \Psi_{\ell m}(t,r) \sim e^{-i\omega(t-r_*)}\,, \quad \text{(pure outgoing waves)}, \;\; \text{for} \quad r_* \to +\infty, \\ \psi_{\ell m\omega}(r) &\sim e^{-i\omega r_*}\,, \quad \Psi_{\ell m}(t,r) \sim e^{-i\omega(t+r_*)}\,, \quad \text{(pure ingoing waves)}, \;\; \text{for} \quad r_* \to -\infty. \end{aligned} \tag{44}$$

The above conditions in eq. (44) ensure that energy flows into the black hole at r_H and out across the cosmological horizon r_Λ. By applying the boundary conditions, the eigensolutions of eq. (41) are found with a discrete set of QNM frequencies ω_n. The imaginary part of the QNM frequency determines how fast the perturbation field is damped and has to be negative in order for the solution to be dynamically stable. However, the boundary conditions eq. (44) on $\psi_{\ell m\omega}(r)$ also imply that it would grow exponentially to infinity at $r_* \to \pm\infty$. This problem is caused by the singular properties of the Schwarzschild-like coordinates, about which we will discuss in details later in sec. 4. [1]

In the next section we discuss the SdS spacetime from the perspective of the hyperboloidal framework. Not only does this strategy provides a natural geometrical approach to incorporate the boundary conditions eq. (44), but the hyperboloidal framework also offers a clean route to describe the three spacetime limits similar to the geometrical prescription by Geroch [30], as discussed in sec. 4 and sec. 5.

4 Hyperboloidal Framework

The traditional approach to solve the quasinormal modes is performed in the coordinate system of $(t, r_*, \theta, \varphi)$. In such a coordinate system, problem arises when we try to impose the boundary condition at $r_* \to \pm\infty$ due to the singularities of the coordinate system that infinite constant t surfaces accumulate at the spatial infinity i^0 and the bifurcation sphere $\mathcal{B}$. The hyperboloidal coordinate system is free from such coordinate singularity since the hyperboloidal constant time surface will penetrate smoothly into the horizons, as later shown in Fig. 1. From a numerical perspective it is also some extra trouble to deal with the infinite domain $r_* \in (-\infty, \infty)$. The problems are rooted in the choice of the coordinate system we're using, and thus the hyperboloidal coordinate system gained attention over the past decades for its robust geometrical approach to deal with black hole QNM problems. The hyperboloidal framework not only serves as a powerful tool for rigorous mathematical analysis for black hole perturbation, a systematic and robust way of controlling spacetime limits, but also a suitable basis for high efficiency and high accuracy numerical calculations on QNM solutions.

[1] From now on, we will omit the $\ell m\omega$ index for the radial wave function ψ for simplicity.

A generic transformation into hyperboloidal coordinates $(\tau, \sigma, \theta, \varphi)$ [24], in the notation introduce in ref. [25] reads

$$t = \lambda\Big(\tau - H(\sigma)\Big), \quad r = \lambda\frac{\rho(\sigma)}{\sigma}, \tag{45}$$

with λ a typical length scale of the spacetime to be fixed according to the particular spacetime limit under consideration. The height function $H(\sigma)$ and radial function $\rho(\sigma)$ represents degrees of freedom fixing the hyperboloidal slice τ = constant, and the radial compactification. The radial compactification can also be represented in terms of the dimensionless tortoise coordinate

$$x(\sigma) = \frac{r_*(r(\sigma))}{\lambda}. \tag{46}$$

From eq. (25), we observe that the dimensionless tortoise coordinate assumes the form [25]

$$x(\sigma) = x_H(\sigma) + x_\Lambda(\sigma) + x_o(\sigma), \tag{47}$$

with the functions $x_H(\sigma)$ and $x_\Lambda(\sigma)$ singular at the black-hole σ_H and cosmological σ_Λ horizons, respectively. The function $x_o(\sigma)$, on the other hand, is regular in the entire radial domain.

Under the transformation eq. (45), the line element eq. (1) conformally re-scales as

$$\begin{aligned} d\bar{s}^2 &= \sigma^2 ds^2 \\ &= \lambda^2\beta(\sigma)\Big(-p(\sigma)d\tau^2 + 2\gamma(\sigma) + w(\sigma)d\sigma^2\Big) \\ &\quad +\lambda^2\rho(\sigma)^2 d\varpi^2, \end{aligned} \tag{48}$$

with the hyperboloidal metric functions given by [25]

$$\beta(\sigma) = \rho(\sigma) + \sigma\rho'(\sigma), \quad p(\sigma) = -\frac{1}{x'(\sigma)} \tag{49}$$

$$\gamma = p(\sigma)H'(\sigma), \quad w(\sigma) = \frac{1-\gamma(\sigma)^2}{p(\sigma)}. \tag{50}$$

The conformal re-scalling in eq. (48) differs slightly from the one suggested in ref. [25]. Here, we explicitly retain the length scale λ in eq. (48), keeping the conformal line element a quantity with dimension $[ds^2] = (\text{Length})^2$. This choice will play an important role when studying the extremal limit $\eta \to 1$ in sec. 5.3.

To fix the hyperboloidal degrees of freedom, we restrict ourselves to the minimal gauge class [25].

4.1 The minimal gauge

The minimal gauge [25] fixes the radial transformation by imposing $\beta(\sigma)$ = constant, which implies

$$\rho(\sigma) = \rho_0 + \rho_1\sigma. \tag{51}$$

The free parameters ρ_0 and ρ_1 are useful to map specific spacetime hypersurfaces into surfaces at a fixed σ value. Such a freedom provides us with the necessary elements to study the two possible limits $\eta \to 0$, and the extremal limit $\eta \to 1$.

More specifically, there are four spacetime surfaces of particular importance: the singularity $r = 0$, horizons $r = r_H$ and r_Λ, and the asymptotic region $r \to \infty$. Eq. (45) maps them from the set $\{0, r_H, r_\Lambda, \infty\}$ into $\{\sigma_{\rm sing}, \sigma_H, \sigma_\Lambda, 0\}$. Recall that in the original Schwarzschild coordinates, the horizons $r_H(M,\Lambda)$ and $r_\Lambda(M,\Lambda)$ coordinate locations depend parametrically on the mass and cosmological constant, whereas the singularity and the asymptotic region are fixed, respectively, at $r = 0$ and $r \to \infty$, regardless of M and Λ.

In the hyperboloidal coordinates, the asymptotic region is, by construction, fixed at a coordinate ($\sigma = 0$), completely independent from the choice of M and Λ. However, the parameters ρ_0 and ρ_1 offer a freedom to place two of the remaining relevant surfaces at fixed values. As detailed in sec. 5, this freedom is essential to ensure the correct spacetime limits as $\eta \to 0$ or $\eta \to 1$.

To fix the height function in eq. (45), we recall that as $\sigma \to \sigma_H$, the hyperboloidal hypersurface τ =constant must behave as the ingoing null coordinate $\tau \sim v = t + r_*$, whereas for $\sigma \to \sigma_\Lambda$, the surface must behave as the outgoing null coordinate $\tau \sim u = t - r_*$. A straightforward way to ensure this properties is by reverting the sign of $x_\Lambda(\sigma)$ in eq. (47), i.e $H(x) = x_H(\sigma) - x_\Lambda(\sigma) + x_o(\sigma)$. This line of reasoning is in accordance with the in-out strategy [25] and it fixes a hyperboloidal coordinate system for $\eta \neq 0$.

As we will show, however, this strategy *does not yield a well-define limit* to the Schwarzschild geometry as $\eta \to 0$. Instead, one needs to resort to the out-in strategy [25]. In practical terms, this approach amounts to also reverting the sign of the regular term $x_o(\sigma)$ in eq. (47), i.e., the height function is given by

$$H(\sigma) = x_H(\sigma) - x_\Lambda(\sigma) - x_o(\sigma). \tag{52}$$

With the expressions eq. (51) and eq. (52) fixing the the hyperboloidal transformation eq. (45) in the minimal gauge, one can study the limits of the SdS geometry with respect to the parameter η.

The only remaining parameter in eq. (45) is the typical length scale λ, which can be associated either with the horizon or the cosmological length r_H or r_Λ, respectively. Thus, the choice of λ plays an important role in the limiting process, as well. In particular, fixing the unit of length also affects how dimension observables, such as the QNM frequencies ω_n, scale.

4.2 Solving the Quasinormal modes

Since the time slices τ = constant penetrate the black hole and cosmological horizons, the boundary conditions eq. (44) are automatically satisfied. Indeed, as a direct consequence of the coordinate transformation eq. (45) the scalar field $\psi_\ell(r)$ transforms as[2]

$$\psi_\ell(r) = Z(\sigma)\bar{\psi}_\ell(\sigma), \quad Z(\sigma) = e^{sH(\sigma)}, \tag{53}$$

with $Z(\sigma)$ responsible for ensuring eq. (44) [24, 25]. In terms of the field $\bar{\psi}_\ell(\sigma)$, eq. (41) is re-expressed in terms of the eigenvalue problem L [34]

$$\begin{pmatrix} 0 & 1 \\ w^{-1}\boldsymbol{L_1} & w^{-1}\boldsymbol{L_2} \end{pmatrix} \begin{pmatrix} \bar{\psi} \\ \bar{\zeta} \end{pmatrix} = s \begin{pmatrix} \bar{\psi} \\ \bar{\zeta} \end{pmatrix}, \tag{54}$$

with the operators

$$\boldsymbol{L_1} = \frac{d}{d\sigma}\left(p(\sigma)\frac{d}{d\sigma}\right) - \bar{V}_\ell(\sigma), \tag{55}$$

$$\boldsymbol{L_2} = 2\gamma(\sigma)\frac{d}{d\sigma} + \gamma'(\sigma), \tag{56}$$

$$\tag{57}$$

[2]The relation $r(\sigma)$ is assumed in eqs. (53) and (58).

and the re-scaled potential $\bar{V}_\ell$ given by

$$\bar{V}_\ell(\sigma) = \frac{\lambda^2}{p(\sigma)} V_\ell(r). \tag{58}$$

The dimensionless frequency s is fixed by the length scale λ via

$$\lambda\omega = is. \tag{59}$$

As already mentioned, fixing λ with respect to the black hole or cosmological horizon scales will impact how the QNMs behave in the limiting process $\eta \to 0$ or $\eta \to 1$.

5 Spacetime Limits

We will now demonstrate how the hyperboloidal framework provides a clean geometrical strategy to study the limits of the SdS spacetime akin to the rigorous approach by Geroch [30]. In particular, we explore the freedom in eq. (51) given by the parameters ρ_0 and ρ_1 to fix relevant spacetime surfaces at constant coordinate values. Then we will be able to get a natural description of all limits of the SdS spacetime within our geometrical framework, as is demonstrated in Fig. 1.

5.1 The Schwarzschild scenario

In the Schwarzschild scenario, the parameter η is understood as a small deviation from the Schwarzschild geometry. Therefore, the characteristic length scale of the space time is given by $\lambda = r_H$. Moreover, to recover the Schwarzschild geometry as $\eta \to 0$, one must ensure that the black hole horizon is at a fixed surface σ_H, independent of κ.

The most simple choice is to fix the horizon surface at $\sigma_H = 1$, achieved trivially by a the radial transformation eq. (51) with parameters

$$(\rho_0, \rho_1) = (1, 0) \Rightarrow r = \frac{r_H}{\sigma}. \tag{60}$$

Eq. (60) maps the singularity $r = 0$ to $\sigma_{\text{sing}} \to \infty$, whereas the cosmological horizon's depends on the spacetime parameter η directly via $\sigma_\Lambda = \eta$. Therefore, the limit $\eta \to 0$ corresponds to having the cosmological horizon degenerating into future null infinity as $\sigma_\Lambda \to 0$. The top panel of Fig. 1 shows the Penrose diagram illustrating such a process.

This limit corresponds to a discontinuous change in the topology of future null infinity. While the surface $\sigma = 0$ is spacelike for $\eta \neq 0$, it becomes null when $\eta = 0$.

Despite the topology change, the dimensionless tortoise function has a well defined limit as $\eta \to 0$. With the radial compactification eq. (60), the terms in eq. (47) read

$$x_H(\sigma) = \frac{(1+\eta+\eta^2)}{(1-\eta)(2\eta+1)} \ln|1-\sigma|, \tag{61}$$

$$x_\Lambda(\sigma) = -\frac{(1+\eta+\eta^2)}{\eta(1-\eta)(2+\eta)} \ln\left|\frac{\sigma}{\eta} - 1\right|, \tag{62}$$

$$x_o(\sigma) = \frac{(1+\eta+\eta^2)(1+\eta)}{\eta(2\eta+1)(\eta+2)} \ln\left|1 + \sigma\frac{1+\eta}{\eta}\right|. \tag{63}$$

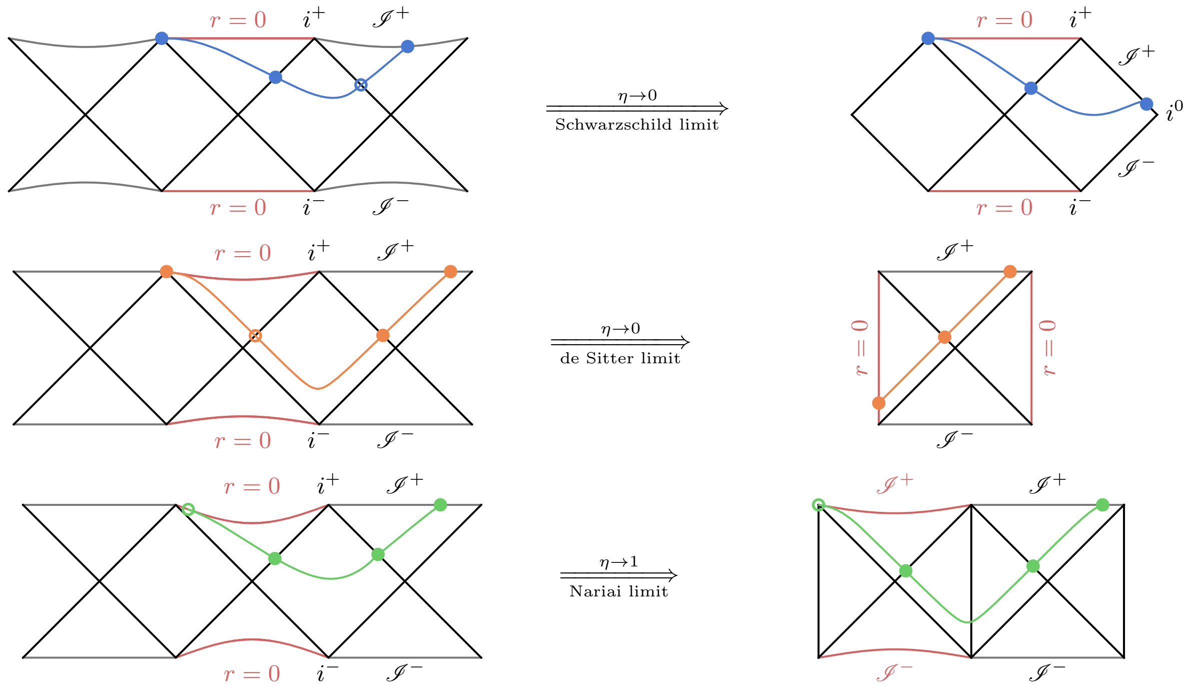

Figure 1: Penrose Diagrams for the Schwarzschild-de Sitter spacetime and their respective limits achieved within the hyperboloidal framework. Solid points represent surfaces with a fixed coordinate value, whereas surfaces with an empty dot move freely in the grid. In all case, $\mathscr{I}^+$ is fixed at a coordinate location $\sigma = 0$. *Top Panel - The Schwarzschild scenario.* The black hole horizon fixes the spacetime length scale $\lambda = r_H$. The event horizon $\mathcal{H}^+$ and the singularity are fixed, but the cosmological horizon is free. The corresponding limit $\eta \to 0$ is the Schwarzschild space time, where the cosmological horizon degenerates into $\mathscr{I}^+$. *Middle Panel - The de Sitter scenario.* The cosmological horizon fixes the spacetime length scale $\lambda = r_\Lambda$. The cosmological horizon $\mathcal{H}^+$ and the singularity are fixed, but the event horizon is free. The corresponding limit $\eta \to 0$ is the de Sitter space time, where the event horizon tends to the surface $r = 0$. *Bottom Panel - The Nariai scenario.* The cosmological and event horizons $\mathcal{H}^+$ are fixed, but the singularity is moves freely. The spacetime length scale incorporates a singular behaviour $\lambda = r_H/(1-\eta)$, but the corresponding limit $\eta \to 1$ is finite into the de Nariai space time.

The function $x_H(\sigma)$ is well behaved at $\eta = 0$. Even though the functions $x_\Lambda(\sigma)$ and $x_o(\sigma)$ individually diverge as $\eta \to 0$, these divergences have exactly opposite signs, i.e.

$$x_\Lambda(\sigma) = -\frac{1}{2\eta}\ln\left(\frac{\sigma}{\eta}\right) + \mathcal{O}(\eta^0), \tag{64}$$

$$x_o(\sigma) = \frac{1}{2\eta}\left(\frac{\sigma}{\eta}\right) + \mathcal{O}(\eta^0). \tag{65}$$

Therefore the contribution from the sum $x_\Lambda(\sigma) + x_o(\sigma)$ is regular as $\eta \to 0$ and one recovers the Schwarzschild expression for the tortoise coordinate [25]

$$\lim_{\eta\to 0} x(\sigma) = \frac{1}{\sigma} - \ln(\sigma) + \ln(1-\sigma). \tag{66}$$

The regularity of the combination $x_\Lambda(\sigma)+x_o(\sigma)$ plays a fundamental role when taking the limit $\eta \to 0$ within the hyperboloidal coordinate system. The height function defined in eq. (52) via the out-in strategy has precisely a factor $-x_\Lambda(\sigma)-x_o(\sigma)$, which ensures a regular Schwarzschild limit into the expected minimal gauge expression in the Schwarzschild spacetime [25]

$$\lim_{\eta\to 0} H(\sigma) = -\frac{1}{\sigma} + \ln(\sigma) + \ln(1-\sigma). \tag{67}$$

However, hyperboloidal foliations may arise from different choices of height functions $H(\sigma)$, some of which with a ill-defined limit $\eta \to 0$. Indeed, as mentioned in sec. 4, the in-out strategy does provide a functioning hyperboloidal coordinate system when $\eta \neq 0$, but the combination $-x_\Lambda(\sigma) + x_o(\sigma) \sim \eta^{-1}$ in the height function has a singular limit $\eta \to 0$.

Eqs. (61) – (63) provides all the necessary ingredients to formulate the QNM eigenvalue problem (54). With $x_H(\sigma)$, $x_\Lambda(\sigma)$ and $x_o(\sigma)$ one constructs $x(\sigma)$ and $H(\sigma)$ in eqs. (47) and (52). From these quantities, the line elements eqs. (49) and (50), as well as the re-scaled potential eq. (58) building up the operator in eq. (54) follow directly. Having fixed the reference length scale to the horizon's size $\lambda = r_h$, the resulting QNM frequencies eq. (59) associated with the configuration appropriated to the Schwarzschild limit are expressed in terms of the dimensionless values

$$\omega^{\rm Sch} = r_H \omega. \tag{68}$$

5.2 The de Sitter scenario

To study the de Sitter scenario, the cosmological horizon is the natural characteristic spacetime length scale $\lambda = r_\Lambda$. Since the parameter η is understood as a small deviation from the de Sitter geometry, one must ensure that the cosmological horizon is fixed at surface σ_Λ, independent of κ.

Similar to the previous section, a simple choice is to fix $\sigma_\Lambda = 1$, which could be easily achieved by a transformation $r = r_\Lambda/\sigma$. As before, this choice pushes the coordinate location of the surface $r = 0$ into $\sigma_{\rm sing} \to \infty$. Apart from that, it also maps the black-hole horizon into the surface $\sigma_h = \eta^{-1}$, which make σ_H divergent in the limit $\eta \to 0$. Such a divergence is consistent with our expectations. For $\eta \neq 0$, $r = 0$ is a spacelike hypersurface corresponding to the BH singularity. As $\eta \to 0$, the black-hole horizon degenerates into the singularity $r = 0$ ($\sigma_{\rm sing} \to \infty$), and the surface $r = 0$ changes topology, becoming a regular timelike hypersurface, representing the origin of the coordinate system.

However, this radial compactification is not optimal for numerical studies, where the numerical domain is defined in the exterior BH region $\sigma \in [\sigma_\Lambda, \sigma_h]$. As $\eta \to 0$, the domain stretches out with σ_h assuming very high values.

To solve this issue, we use the freedom in eq. (51) to map the singularity $r = 0$ into a fixed, but finite coordinate value $1 < \sigma_{\rm sing} < \infty$. By imposing $r(\sigma_{\rm sing}) = 0$ and $r(1) = r_\Lambda$ into the radial eqs. (45) and (51), one obtains

$$(\rho_0, \rho_1) = \left(\frac{\sigma_{\rm sing}}{\sigma_{\rm sing} - 1}, \frac{-1}{\sigma_{\rm sing} - 1}\right) \Rightarrow r = \frac{r_\Lambda}{\sigma}\frac{\sigma_{\rm sing} - \sigma}{\sigma_{\rm sing} - 1}. \tag{69}$$

In this way, the coordinate location of the event horizon becomes

$$\sigma_H = \frac{\sigma_{\rm sing}}{1 + \eta(\sigma_{\rm sing} - 1)}, \tag{70}$$

and as expected, $1 < \sigma_H = \sigma_{\rm sing} < \infty$ when $\eta = 0$. The process is demonstrated in the middle panel of Fig. 1.

With eq. (69) substituted into eq. (28) on reads the individual terms of the dimensionless tortoise coordinate

$$\begin{aligned} x_H(\sigma) &= \frac{\eta\,(1+\eta+\eta^2)}{(1+2\eta)(1-\eta)} \ln\left|1 - \eta\sigma\frac{\sigma_{\rm sing} - 1}{\sigma_{\rm sing} - \sigma}\right|, & (71)\\ x_\Lambda(\sigma) &= -\frac{(1+\eta+\eta^2)}{(\eta+2)(1-\eta)} \ln\left|1 - \sigma\frac{\sigma_{\rm sing} - 1}{\sigma_{\rm sing} - \sigma}\right|, & (72)\\ x_o(\sigma) &= \frac{(1+\eta)(1+\eta+\eta^2)}{(2+\eta)(1+2\eta)} \\ &\quad \times \ln\left|1 + (1+\eta)\sigma\frac{\sigma_{\rm sing} - 1}{\sigma_{\rm sing} - \sigma}\right|. & (73) \end{aligned}$$

All these terns have a well-defined limit $\eta \to 0$, in particular with $x_H(\sigma) \to 0$. Thus, the dimensionless tortoise coordinate and the height function in the de Sitter spacetime becomes

$$\lim_{\eta\to 0} x(\sigma) = -\lim_{\eta\to 0} H(\sigma) = \frac{1}{2}\ln\left|\frac{\sigma_{\rm sing} + \sigma\,(\sigma_{\rm sing} - 2)}{\sigma_{\rm sing}(\sigma - 1)}\right|. \tag{74}$$

Without loss of generality we fix the parameter $\sigma_{\rm sing} = 2$, which simplifies the above a results.

Eq. (74) shows that at $\eta = 0$, the height function coincides with the tortoise function up to an overall minus sign. This result implies that the time hypersurfaces τ =constant becomes an outgoing null coordinate as $\eta \to 0$, when the hyperboloidal coordinate is constructed within the out-in minimal gauge strategy according to eq. (52).

As in the previous section, eqs. (71) – (73) provide all the elements to formulate the QNM eigenvalue problem (54). However, the setup appropriated to the dS limit has $\lambda = r_\Lambda$ as the reference length scale, so the resulting dimensionless QNM frequencies (59) are

$$\begin{aligned} \omega^{\rm dS} &= r_\Lambda \omega \\ &= \eta^{-1}\omega^{\rm Sch}. & (75) \end{aligned}$$

5.3 The Nariai scenario

Neither of the previous configurations is appropriate to study the extremal limit $\eta \to 1$. In both cases, eqs. (61) – (63) or eqs. (71) – (73) yield a line element (48) behaving as

$$\bar{g}_{\tau\sigma} \sim (1-\eta)^{-1}, \quad \bar{g}_{\sigma\sigma} \sim (1-\eta)^{-2}. \tag{76}$$

This result is not surprising, as it reflect the degeneracy of the horizon coordinate values $r_H = r_\Lambda = r_{\rm ext}$ with

$$r_{\rm ext} = 3M = \sqrt{\Lambda^{-1}}. \tag{77}$$

In the Schwarzschild scenario, the coordinate value for the cosmological horizon $\sigma_\Lambda(\eta)$ depends explicitly on the parameter η, with the two surfaces degenerating in the limit $\eta \to 1$, i.e., $\sigma_\Lambda(1) = \sigma_h = 1$. The same occurs in the de Sitter scenario, now with the black hole coordinate value $\sigma_h(\eta)$ having the explicit η dependence. The limiting process shows the same degeneracy $\sigma_h(1) = \sigma_\Lambda = 1$.

To properly obtain the spacetime in the extremal limit $\eta \to 1$, one must map the two horizons r_H and r_Λ into two distinct hypersurfaces $\sigma_h \neq \sigma_\Lambda$, fixed at coordinate values independent of the parameter η. Without loss of generality, we can keep the event horizon at $\sigma_h = 1$, and fix the cosmological horizon at the value $\sigma_\Lambda = 1/2$. By imposing $r(1) = r_H$ and $r(1/2) = r_\Lambda$ for $\eta \neq 1$ into the radial eqs. (45) and (51), we obtain

$$(\rho_0, \rho_1) = \left(\frac{r_H(1-\eta)}{\lambda\eta}, -\frac{r_H(1-2\eta)}{\lambda\eta} \right), \tag{78}$$

$$r = \frac{r_H\Big((1-\sigma) - \eta(1-2\sigma) \Big)}{\eta\sigma}. \tag{79}$$

In the limit $\eta \to 1$, the above transformation is actually singular since eq. (79) reduces to $r(\sigma) = r_H$. This behaviour is well-known, and typical for obtaining the near-horizon geometry of extremal black holes [35]. A regular spacetime arises once one combines the singular radial transformation (79) with a singular map in the time coordinate $t \to t/(1-\eta)$. As we will show, the characteristic length scale λ will incorporate the troublesome factor $(1-\eta)$. Indeed, eq. (79) determines the individual terms of the dimensionless tortoise coordinate

$$\begin{aligned}
x_H(\sigma) &= \frac{r_H\,(1+\eta+\eta^2)}{\lambda(1+2\eta)(1-\eta)} \ln|1-\sigma|, && (80)\\
x_\Lambda(\sigma) &= -\frac{r_H\,(1+\eta+\eta^2)}{\lambda\eta(2+\eta)(1-\eta)} \ln|2\sigma-1|, && (81)\\
x_o(\sigma) &= \frac{r_H(1+\eta)\,(1+\eta+\eta^2)}{\lambda\eta(1+2\eta)(2+\eta)} \ln\left|1+\frac{3\eta\sigma}{1-\eta}\right|. && (82)
\end{aligned}$$

As a consequence, the dimensionless tortoise coordinate and height function behave as

$$\begin{aligned}
x &= \frac{r_H}{\lambda(1-\eta)}\left(\ln\left|\frac{2\sigma-1}{1-\sigma}\right| + \mathcal{O}(1-\eta) \right), && (83)\\
H &= \frac{r_H}{\lambda(1-\eta)}\Big(\ln|(2\sigma-1)(1-\sigma)| + \mathcal{O}(1-\eta) \Big). && (84)
\end{aligned}$$

To ensure a well-behaved limit $\eta \to 1$, one must set the characteristic length scale to

$$\lambda = \frac{r_H}{1-\eta}. \tag{85}$$

A similar argument follow from the line element (48), as its components behave as

$$\begin{aligned}
\bar{g}_{\tau\tau} &= -\lambda^2(1-\eta)^2\Big((1-\sigma)(2\sigma-1) + \mathcal{O}(1-\eta) \Big), && (86)\\
\bar{g}_{\tau\sigma} &= \lambda r_H(1-\eta)\Big((3-4\sigma) \Big), && (87)\\
\bar{g}_{\sigma\sigma} &= 8r_H^2 + \mathcal{O}(1-\eta). && (88)
\end{aligned}$$

With eq. (85), the limit $\eta \to 1$ yields the dimensionless physical metric for the Nariai spacetime in hyperboloidal coordinates, if we recognize the black hole horizon r_H as the Nariai horizon r_E,

$$\begin{aligned}\frac{ds^2}{r_E^2} &= -\frac{(1-\sigma)(2\sigma-1)}{\sigma^2}d\tau^2 \\ &\quad +\frac{2(3-4\sigma)}{\sigma^2}d\sigma d\tau + \frac{8}{\sigma^2}d\sigma^2 + d\varpi^2,\end{aligned} \tag{89}$$

The limiting strategy outlined so far provides all the necessary tools to calculate QNMs as the eigenvalue problem eq. (54) up to $\eta = 1$. However, the choice for a characteristic length scale as eq. (85) implies that the dimensionless QNM frequencies in extremal limiting scenario scale as

$$\begin{aligned}\omega^{\text{ExtLimit}} &= \frac{r_H\omega}{1-\eta} \\ &= \frac{\omega^{\text{Sch}}}{1-\eta}\end{aligned} \tag{90}$$

compared to the frequencies with respect to SdS time.

To verify that Eq. (89) indeed corresponds to the Nariai spacetime, we considers the Nariai line element in its tradional form

$$ds_N^2 = -\frac{r_E^2 - r_N^2}{r_E^2}dt_N^2 + \frac{r_E^2}{(r_E^2 - r_N^2)}dr_N^2 + r_E^2 d\varpi^2. \tag{91}$$

Then, the hyperboloidal transformation could be found by our strategy introduced in sec. 4.1, when we map the horizons $\{r_E, -r_E\}$ into $\{1/2, 1\}$. With the characteristic length scale $\lambda = r_E/2$, the coordinate transformation reads

$$\begin{aligned}\frac{t_N}{r_E} &= \frac{1}{2}\left(\tau - h(\sigma)\right), \quad h(\sigma) = \ln(1-\sigma) + \ln\left(\sigma - \frac{1}{2}\right), \\ \frac{r_N}{r_E} &= \frac{2}{\sigma} - 3,\end{aligned} \tag{92}$$

which indeed transforms the line element eq. (91) into eq. (89). The bottom panel of Fig. 1 illustrates this limiting process from SdS spacetime to Nariai spacetime. In this context, the extremal limit frequencies will be related to the Nariai frequencies ω_N in traditional form as

$$\omega^{\text{ExtLimit}} = \frac{r_E}{2}\omega_N \tag{93}$$

with our length scale $\lambda = r_E/2$.

The QNM problem of the aforementioned spacetimes in this subsection is solved analytically, by dealing with the PDE of the scalar field $\Psi(x)$ in the time domain. The scalar field's wave equation is determined by the Klein-Gordon equation $\Box\Psi = 0$, or a more detailed form which is useful in our calculations

$$\frac{1}{\sqrt{-g}}\partial_\mu\left(\sqrt{-g}g^{\mu\nu}\partial_\nu\Psi\right) = 0. \tag{94}$$

The line element in the form of eq. (91) would then yield the wave equation

$$\begin{aligned}&\left\{(1-\frac{r_N^2}{r_E^2})\frac{\partial}{\partial(r_N/r_E)}\left[(1-\frac{r_N^2}{r_E^2})\frac{\partial}{\partial(r_N/r_E)}\right]\right. \\ &\left. -\frac{\partial^2}{\partial(t_N/r_E)^2} - l(l+1)(1-\frac{r_N^2}{r_E^2})\right\}\Psi_\ell = 0\end{aligned} \tag{95}$$

with a standard separation of variables in terms of the spherical harmonics $\Psi(t_N, r_N, \theta, \varphi) = \Psi_\ell(t_N, r_N) Y_{\ell m}(\theta, \varphi)$.

One could easily transform eq. (95) into the Pöschl-Teller form in ref. [36] through the dimensionless tortoise coordinates,

$$\tilde{T} = \frac{t_N}{r_E}, \quad \tilde{X} = \tanh^{-1}(\frac{r_N}{r_E}). \tag{96}$$

The wave equation will then read

$$\left(\frac{\partial^2}{\partial \tilde{T}^2} - \frac{\partial^2}{\partial \tilde{X}^2} + \frac{U_0}{\cosh^2 \tilde{X}}\right) \Psi_\ell(\tilde{T}, \tilde{X}) = 0, \tag{97}$$

where we have the Pöschl-Teller potential with $U_0 = l(l+1)$, and $\Psi_\ell(\tilde{T}, \tilde{X})$ is the coefficients when $\Psi(t_N, r_N, \theta, \varphi)$ is decomposited with spherical harmonics $Y_{\ell m}(\theta, \varphi)$.

To find the analytical solution of eq. (97), we follow the strategy in ref. [34] with a coordinate transformation

$$\begin{aligned} T &= \tilde{T} + \frac{1}{2} \ln(1 - \tanh(\tilde{X})^2), \\ X &= \tanh(\tilde{X}). \end{aligned} \tag{98}$$

Then the wave equation will be transformed into a second order linear PDE,

$$\begin{aligned} \Big(\partial_T^2 &+ 2X \partial_T \partial_X + \partial_T + 2X \partial_X \\ &- (1 - X^2)\partial_X^2 + U_0\Big) \Psi_\ell(T, X) = 0. \end{aligned} \tag{99}$$

With a Fourier transformation in T, eq. (99) becomes a second order linear ODE with three singular points at -1, 1 and ∞. Such equation could be solved analytically with the Gaussian hypergeometric function as in the works of ref. [34]

$$\begin{aligned} \Psi_\ell(T, X) &= {}_2F_1(a, b\,; c\,; z) e^{i\omega_{PT} T}, \quad X = 1 - 2z, \\ a,\ b &= \frac{(2i\omega_{PT} + 1) \pm i\sqrt{4U_0 - 1}}{2}, \quad c = 1 + i\omega_{PT}, \end{aligned} \tag{100}$$

and the Nariai frequencies are therefore determined as

$$\begin{aligned} \omega_N &= r_E^{-1} \omega_{\mathrm{PT}} \\ &= r_E^{-1} \left(\pm \frac{\sqrt{4U_0 - 1}}{2} + i \left(n + \frac{1}{2} \right) \right) \end{aligned} \tag{101}$$

when we force the hypergeometric series to be truncated into a polynomial to meet the regularity conditions of the QNM solutions.

In a straightforward manner, eq. (99) could also be derived if we start from the wave equation eq. (94) of the SdS extremal spacetime eq. (89)

$$\begin{aligned} \Big\{ 8\partial_\tau^2 &- (2(3 - 4\sigma)\partial_\sigma - 4)\partial_\tau + (-1 + \sigma)(-1 + 2\sigma)\partial_\sigma^2 \\ &+ (-3 + 4\sigma)\partial_\sigma + \frac{l(l+1)}{\sigma^2} \Big\} \Psi_\ell(\tau, \sigma) = 0, \end{aligned} \tag{102}$$

and apply the combined coordinate transformations eq. (92), eq. (96), and eq. (98)

$$T = \frac{1}{2}\left(\tau - 2\log\sigma + \log 8\right), \quad X = \frac{2}{\sigma} - 3, \tag{103}$$

then we will recover the form of eq. (99) as we expected. It is clear in eq. (103) the factor of 1/2 in the time coordinate transformation leads to the same overall factor we observe between the SdS extremal frequencies and Pöschl-Teller frequencies as in eq. (93) and eq. (101).

6 Spectral Methods

The (pseudo-)spectral methods are a powerful tool in numerical analysis, where we truncate the infinite series expansion of a function $f(x)$ by N basis functions as a numerical approximation.

$$f(x) = \sum_{i=0}^{N} c_i^{(N)}\phi_i(x) + R^{(N)}(x), \tag{104}$$

where N is the expansion order, $c_i^{(N)}$ are the spectral coefficients, and $R^{(N)}(x)$ is the residual term. As per the collocation point method, for a set of discrete grid points ξ_k where $k = 0, \ldots N$, imposing a vanishing residual term leads to

$$f(\xi_k) = \sum_{i=0}^{N} c_i^{(N)}\phi_i(\xi_k), \quad \text{or} \quad f_k = \sum_{i=0}^{N} \phi_{ki}\, c_i^{(N)}. \tag{105}$$

By inversing the matrix ϕ_{ki} we could find the spectral coefficients $c_i^{(N)}$. Therefore we get an approximation of $f(x)$ of order N by

$$\tilde{f}(x) = \sum_{i=0}^{N} c_i^{(N)}\phi_i(x). \tag{106}$$

To solve the QNM eigenvalue problem (54) we employ a collocation point spectral method having the Chebyshev polynomials of the first kind as a set of basis approximating the underlying functions. For that purpose, we fix a numerical resolution N and introduce the Chebyshev-Lobbato grid

$$\chi_i = \cos\left(\frac{\pi i}{N}\right), \quad i \in \{0, 1, \ldots, N\}. \tag{107}$$

parametrising the domain $\chi \in [-1, 1]$, where the Chebyshev polynomials of first kind $T_k(\chi)$ are defined. By imposing that the approximated functions are exactly represented at the grid points (107) one can represent the derivative operator ∂_χ by the differentiation matrix

$$\mathbb{D}_\chi^{ij} = \begin{cases} -\dfrac{2N^2+1}{6} & , \quad i = j = N \\ \dfrac{2N^2+1}{6} & , \quad i = j = 0 \\ -\dfrac{\chi_j}{2(1-\chi_j)^2} & , \quad 0 < i = j < N \\ \dfrac{\alpha_i}{\alpha_j}\dfrac{(-1)^{i-j}}{\chi_i - \chi_j} & , \quad i \neq j \end{cases}, \tag{108}$$

where

$$\alpha_i = \begin{cases} 2 & , \quad i \in \{0, N\} \\ 1 & , \quad i \in \{1, \ldots, N-1\} \end{cases}. \tag{109}$$

The hyperboloidal radial coordinates, however, are defined in $\sigma \in [\sigma_\Lambda, \sigma_H]$. Typically, a linear map

$$\sigma(\chi) = \sigma_h \frac{1+\chi}{2} + \sigma_\Lambda \frac{1-\chi}{2} \tag{110}$$

$\sigma(\chi)$ from the spectral coordinate χ into σ is employed, but as we will discuss, this choice is not ideal to explore configuration in the limit $\eta \to 0$.

Indeed, the functions in the wave equations, such as the conformal potential $\bar{V}_\ell$, develop strong gradient around the domain boundaries as $\eta \to 0$. The left panel of Fig. 2 displays the conformal potential $\bar{V}_\ell$ with eq. (58) calculated with the Schwarzschild scenario. Since future null infinity $\sigma = 0$ and the cosmological $\sigma_\Lambda(\eta)$ are close to each other as $\eta \to 0$, $\bar{V}_\ell$ develops strong gradients around $\sigma = \sigma_\Lambda$. The plot brings examples for the cases $\eta = 1/3, 1/10$ and $1/100$ where the effect becomes visible. The inset shows the corresponding spectral coefficients obtained when the linear map (110) is employed. One observes a significant loss of accuracy as $\eta \to 0$. An accurate numerical result for the QNMs would then require increasing the numerical truncation parameter N to prohibitive high values. A similar effect happens also in the de Sitter scenario, as shown in the right panel of Fig. 2. In this case, however, strong gradients develop around the value $\sigma = \sigma_{\rm sing}$ (here $\sigma_{\rm sing} = 2$) because the black hole horizon $\sigma_h(\eta)$ approaches $\sigma_{\rm sing}$ as $\eta \to 0$.

Thus, to enhance the numerical solver, we introduce the so-called analytical mesh-refinement (AnMR), which we discuss in the next section.

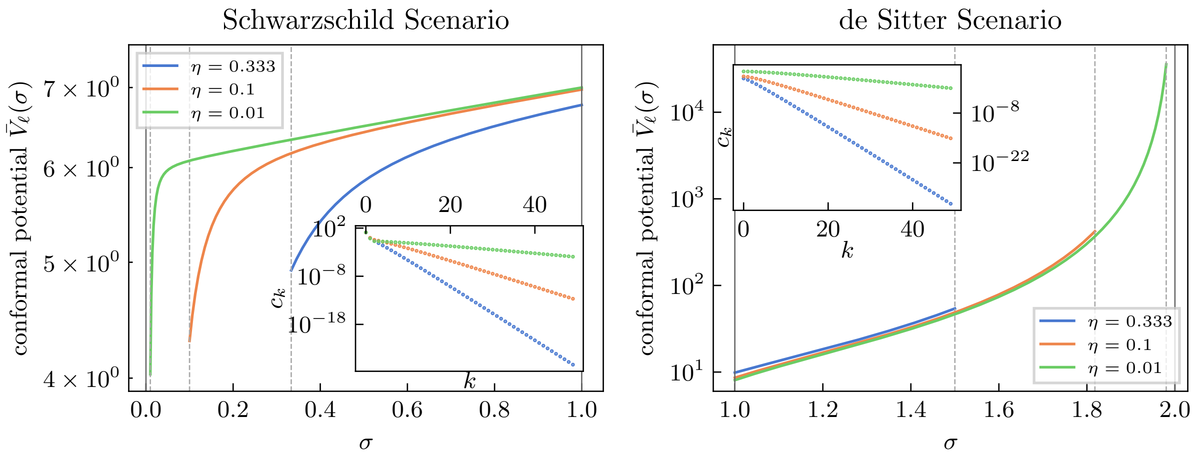

Figure 2: The conformal potential $\bar{V}_\ell(\sigma)$ develops strong gradients in around the horizons as $\eta \to 0$. In the Schwarzschild scenario (left panel), the strong gradient develop around the cosmological horizon as σ_Λ approaches future null infinity. In the de Sitter scenario, it develops around the event horizon as σ_h approaches the singularity. The inset figures show the rate of convergence of the corresponding spectral coefficients representing $\bar{V}_\ell(\sigma)$ without AnMR. As $\eta \to 0$, the strong gradient near the horizons yields a loss of accuracy, which forces one to allocate much more computing power to get a proper accuracy for a QNM solver.

6.1 Analytical Mesh Refinement

Instead of using the linear map (110), we now consider the relation

$$\sigma(\chi) = \sigma_h \frac{1+x(\chi)}{2} + \sigma_\Lambda \frac{1-x(\chi)}{2}, \tag{111}$$

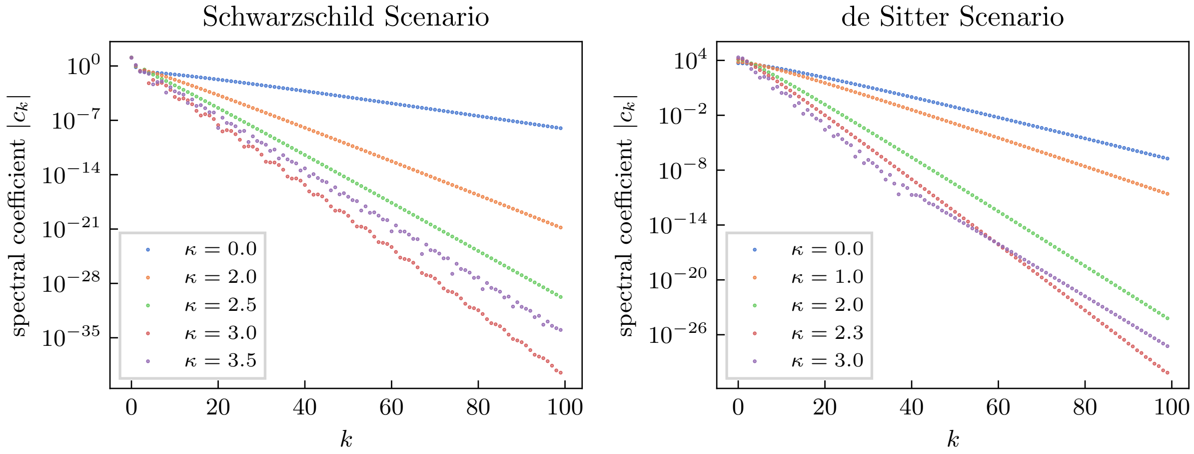

Figure 3: The optimization of the AnMR parameter κ based on the convergence rate of spectral coefficients representing the conformal potential $\bar{V}_\ell(\sigma)$. Both panels illustrate the case for $\eta = 1/100$. Different values of the AnMR parameter κ are tested numerically for the best accuracy in each case. The numerical test shows the optimized values roughly as $\kappa \approx 3.0$ for the Schwarzschild scenario (left panel). For the the de Sitter scenario the best value $\kappa \approx 2.3$ is qualitatively close $\kappa = 3$, which allows to assume the generic scaling (113).

with $x(\chi)$ the AnMR mapping the interval $[-1, 1]$ into itself via

$$x = x_{\rm B}\left(1 - \frac{2\sinh\left[\kappa(1 - x_{\rm B}\chi)\right]}{\sinh(2\kappa)}\right), \tag{112}$$

When $\kappa \to 0$, one recovers the identity $x(\chi) = \chi$. For $\kappa > 0$, $x(\chi)$ accumulates the grid points towards the left boundary for $x_{\rm B} = -1$, or the right boundary for $x_{\rm B} = 1$.

Fig. 3 brings the spectral coefficients associated with the conformal potential $\bar{V}_\ell(\sigma)$ for the Schwarzschild scenario (left panel) and de Sitter scenario (right panel) for $\eta = 1/100$. Without the AnMR ($\kappa = 0$), these coefficients are of order $c_k \sim 10^{-6}$ for a rather high numerical resolution $N = 100$. As κ increases and grid points accumulate around the region with steep gradients, we obtain an enhanced convergence rate up to an optimal value κ_*. For values $\kappa > \kappa_*$, the convergence rate gets worse. A systematic studied of the parameter κ for the Schwarzschild scenario yields the relation for the optimal value as

$$\kappa_*(\eta) = 1 - \ln\eta. \tag{113}$$

In the de Sitter scenario, the optimal parameter κ_* assumes values slightly bellow the relation in eq. (113). However, as displayed in the right panel of fig. 3 for $\eta = 1/100$, the results arising from (113) $\kappa = 3$ are qualitatively similar to the optimal value $\kappa_* = 2.3$. Hence, one can also use the model (113) in the de Sitter scenario, and avoid a tedious optimisation procedure for each individual η.

With the AnMR mappings (111) and (112), one then obtains a discrete representation for the derivative operator ∂_σ via

$$\mathbb{D}_\sigma = \overrightarrow{J^{-1}} \circ \mathbb{D}_\chi, \quad \left(\overrightarrow{J^{-1}}\right)_i = \frac{1}{d\sigma(\chi_i)/d\chi}. \tag{114}$$

with the circle $\circ$ denoting the Hadamard (element-wise) product. Second order derivates follow directly from the product between two matrices $\mathbb{D}_\sigma$. With the discrete representation of the derivative operators, one can approximate the operators (54), (55) and (56) via matrices. The QNM then correspond directly to the eigenvalues of the resulting matrix.

The ultimate test about the use of the AnMR for an efficient calculation of the QNMs is given by studying their numerical convergence.

7 Results

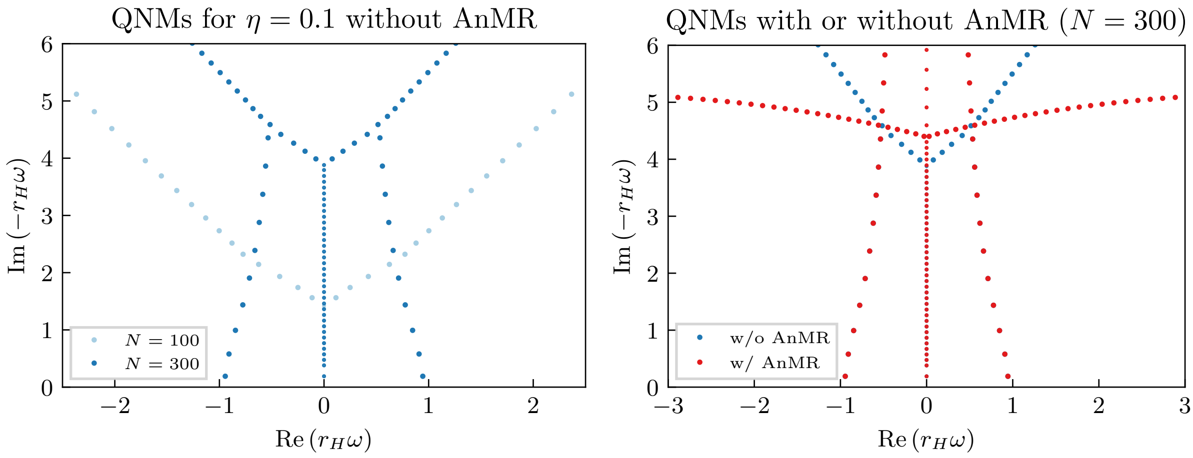

Figure 4: *Top panel:* Light ring and the de Sitter QNM modes resolved without AnMR, under numerical resolutions of $N = 100$ (light blue) and $N = 300$ (dark blue). A "noise brunch" in a V shape emanates from given critical value at the imaginary axis. Reliable data only exist under the "noise" branch, which increases with numerical resolution. *Bottom panel:* Comparison of QNM values with or without AnMR (red and blue, respectively), for numerical resolution $N = 300$. The "noise" branch changes its shape but the offset remains at same order of magnitudes. The AnMR technique allows us to calculate the light ring modes more accurately and we also find further values of light ring modes beyond the noise branch. The de Sitter modes are still valid only below the noise branch, but their evaluation is more precise, see Fig. 5.

In this section we present the results for the SdS QNMs. We begin by discussing the effects of the AnMR as an innovative numerical technique to calculate QNMs in extreme limiting conditions. For that purpose, a systematic convergence analysis is performed. Then, we explore the QNMs limiting behaviour, with the studies divided into the two families of QNMs: the light ring (LR) and the de Sitter (dS) modes.

7.1 Convergence tests

The calculated solutions of the eigenvalue problem (54) are shown in Fig. 4, for a configuration with a moderate value of $\eta = 0.1$. The calculated solutions without AnMR are displayed in the top panel with the numerical resolutions $N = 100$ (light blue) and $N = 300$ (dark blue). In the figure we identify the two families of physical QNMs: the LR and dS modes. Their values agree with the literature up to a region delimited by spurious data point, which we dubbed "noise branch". This noise branch starts at a given critical value at the imaginary axis, spreading across the complex plane in a sort of V shape, and reliable data only exist under the "noise" branch. We observe that this critical value increases with the numerical resolution, so that further physically relevant QNMs are calculated.

When we turn on the AnMR as shown in the bottom panel of Fig. 4, the noise branch changes slightly the shape, but stays at the same order. However, we also obtain data points above the noise. In particular, we are able to calculate more physically relevant values for the

LR modes, while the pure imaginary points above the "noise" branch do not correspond to the de Sitter modes, as they don't agree with predictions and they don't converge with numerical resolution N.

After such qualitative study, we proceed to a more detailed convergence test of the corresponding numerical values. The internal consistency of our numerical methods are examined through convergence tests. To see how the numerical results change with numerical resolution, the maximum resolution that we have is used as a reference $N_{\rm ref}$. The numerical values of quasinormal modes $\omega_n\left(N;\eta\right)$ computed at different resolutions are compared against the results of the reference resolution. The numerical error is therefore defined as

$$\varepsilon_n\left(N;\eta\right) = \left|1 - \frac{\omega_n\left(N;\eta\right)}{\omega_n\left(N_{\rm ref};\eta\right)}\right|, \tag{115}$$

where the index n refers to the n-th mode. Then we can depict the numerical error as a function of resolution. We choose scalar perturbation as an example for the following demonstration, and the angular mode of the potential is fixed as $l = 2$. The maximum numerical resolution is setup as $N = 300$.

We first focus on the convergence rates of LR modes. The top panel of Fig. 5 shows the results without the AnMR, where the dot markers represent the fundamental mode $n = 0$, and the plus markers represent the first overtone $n = 1$. The result of $\eta = 0.5$ (blue) shows a very rapid convergence rate, with error dropping ~ 30 order of magnitude when N goes from 20 to 60. For $\eta = 0.1$ (orange) the accuracy is still acceptable, from order $\sim 10^{-5}$ to $\sim 10^{-10}$, but one clearly observes how the convergence rate worsens. As $\eta \to 0$, the convergence rate gets even worse. Besides, the noise branch starts at very low values around $\omega \sim 0$, contaminating the extraction of QNM overtones. Thus, the numerical calculation eventually becomes prohibitive as it requires rather high numerical resolution N to achieve a moderate accuracy for a meaninful set of QNMs.

Fig. 5's middle panel shows the result with the AnMR implemented. The result of $\eta = 0.1$ (orange) has a much better convergence rate, going to the order of $\sim 10^{-30}$ near $N = 60$. We are also able to calculate the results with smaller values of $\eta = 0.01$ (green) and $\eta = 0.001$ (red) with a decent convergence rate. This allows us to accurately calculate scenarios with $\eta \to 0$. We observe the same behaviour for the de Sitter modes, whose results with AnMR are illustrated in the bottom panel of Fig. 5.

Even though these convergence tests were performed only within the setup adapted to the Schwarzschild limit, cf. Sec. 5.1, the same conclusions are also valid in the case of the Sitter scenario. Indeed, for $\eta \neq 0$ the QNMs calculated in either setup are related to each other only by an overall re-scaling factor as in Eq. (75). Hence, the relative error (115) remains unchanged.

With the geometry and numerics optimised to study the limiting cases of the SdS spacetime, we proceed to a comprehensive study of LR and dS modes in the limit $\eta \to 0$ and $\eta \to 1$ from the perspective of QNM spectra instability.

7.2 Limits into Schwarzschild and de Sitter spacetimes

As described in sec. 5, the resulting spacetime in the limit $\eta \to 0$ depends on how the geometry is fixed via the hyperboloidal foliation, and it may lead either to the Schwarzschild or de Sitter spacetimes. The LR modes are characteristic QNMs in the former geometry, whereas the dS modes characteristic frequencies in the latter. Here, we scrutinise the behaviour of LR and dS modes in the limit $\eta \to 0$ as we approach either the Schwarzschild spacetime or the de Sitter spacetime (sec. 5.1 and sec. 5.2, respectively).

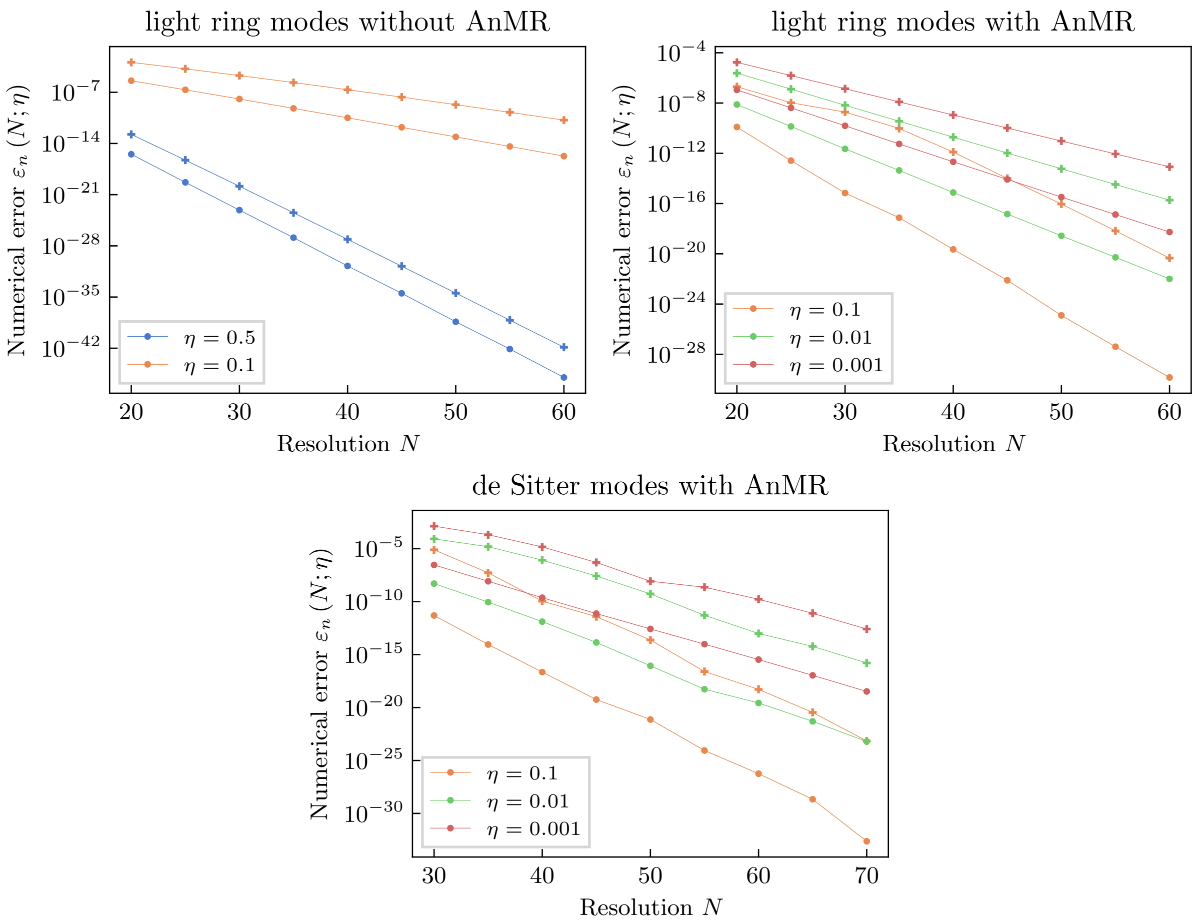

Figure 5: The convergence tests for QNMs, with dot markers representing the fundamental mode $n = 0$, while plus markers the first overtone $n = 1$. Color codes are kept for each value of η across panels. *Top panel* Converge results for light ring modes without AnMR. Though exponential, the convergence rate reduces significantly for as $\eta \to 0$ b) Middle panel shows the same content except that the light ring modes are calculated with AnMR. c) Bottom panel shows the test results of de Sitter modes with AnMR applied. The AnMR significantly enhances the numerical convergence of both light ring and de Sitter modes, with particular relevance for the limit $\eta \to 0$.

To distinguish the two family of QNMs, each of them studied within the two limiting scenarios, we employ the following notation, summirised in Table 7.2. As defined in secs. 5.1 and 5.2, upper script text as in ω^{Sch} and ω^{dS} referes to the underlying geometrical scenario the limit is being take, see eq. (68) and (75); lower script text refers to the particular family of QNMs, either the light ring modes ω_{LR} or the de Sitter modes ω_{dS}.

Table 1: Notation for QNMs values

	Schwarzschild Scenario	de Sitter Scenario
Light Ring modes	$\omega^{\mathrm{Sch}}_{\mathrm{LR}}$	$\omega^{\mathrm{dS}}_{\mathrm{LR}}$
de Sitter modes	$\omega^{\mathrm{Sch}}_{\mathrm{dS}}$	$\omega^{\mathrm{dS}}_{\mathrm{dS}}$

7.2.1 Light ring modes

In the Schwarzschild limiting scenario, the light ring modes converge to the corresponding modes we could find in pure Schwarzschild spacetime. This is what we expect as the stability of the light ring modes in the sense that a small deviation from Schwarschild spacetime to Schwarschild-de Sitter spacetime will lead to small deformation of light ring modes.

In Fig. 6 (left panel) we could see the smooth deformation of light ring modes with the parameter η tracking the geometry of the spacetime. Such deformation is defined as $\delta\omega_n(\eta) = \dfrac{|\omega_n(\eta) - \omega_n(0)|}{|\omega_n(0)|}$ as a function of η, where the QNMs discussed here are $\omega_{\mathrm{LR}}^{\mathrm{Sch}} = r_H \omega_{\mathrm{LR}}$ with r_H used as the typical length scale.

As per our numerical results, we find the following linear relation between the deformation of the light ring modes $\delta\omega_n(\eta)$ and the de Sitter parameter Λ to the leading order, as shown in Fig. 6 (left panel):

$$\delta\omega_n(\eta) \sim \eta^2 \sim \Lambda. \tag{116}$$

This could be seen as the stability of the light ring family of QNMs under the perturbation of a small Λ.

According to the relation in eq. (75), the light ring modes calculated in de Sitter limiting scenario must scale as $\mathcal{O}\left(\eta^{-1}\right)$, as shown in Fig. 6 (right panel). In this way, it is a case of QNM instability where a small deviation from pure de Sitter spacetime introduces a whole new family of QNMs coming from the infinity.

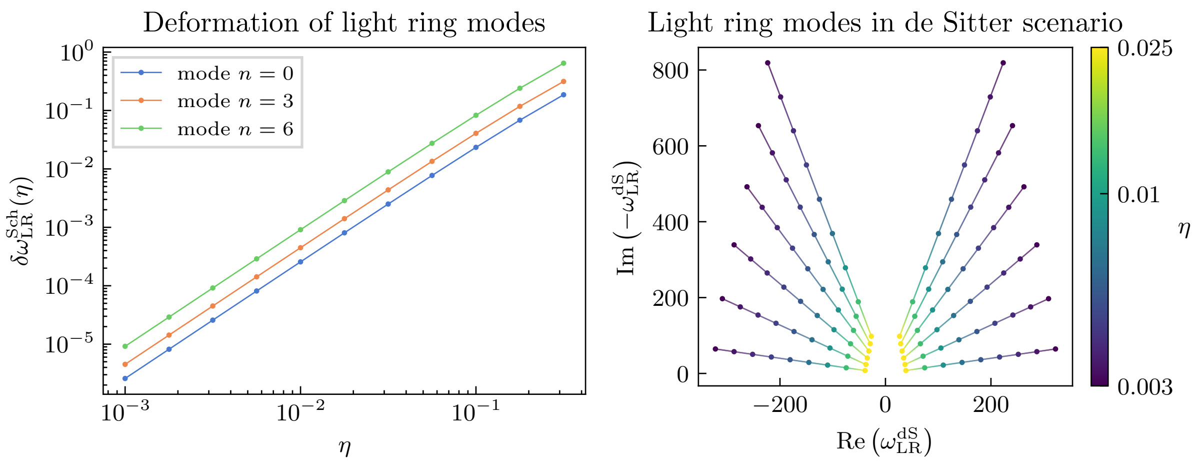

Figure 6: *Left Panel:* Deformation of the light ring modes as a function of η with the typical length scale r_H. Deformations of all different overtones scale roughly as η^2, with slightly different coefficients. The numerical resolution is set up with $N = 300$ here. *Right Panel*: Behaviour of QNMs in the limit $\eta \to 0$ when calculating either within the Schwarzschild scenario, or de Sitter scenario according to scaling given by eq. (75). The light ring modes must diverge as $\mathcal{O}\left(\eta^{-1}\right)$ when calculated within the de Sitter scenario as η approaches 0, because these modes are finite when calculated in the Schwarzschild scenario. In a word, the light ring modes are stable with η added as a perturbation on Schwarzschild spacetime.

7.2.2 de Sitter modes

In the context of de Sitter limiting scenario, the parameter η represents a small deviation from the de Sitter geometry. The de Sitter modes are stable in the sense that a small η leads to small deviation of the de Sitter family of QNMs, see Fig. 7 (left panel). According to the relation in Eq. (75), the difference in ω^{Sch} and ω^{dS} is only a factor of η. Therefore, the dS modes in Schwarzschild limiting scenario must shrink to $\omega = 0$ as $\mathcal{O}(\eta)$ when $\eta \to 0$, see Fig. 7 (right panel).

For $\eta = 0$, the pure Schwarzschild spacetime as a geometrical limit of the Schwarzschild-de Sitter spacetime does not have the family of de Sitter modes, instead it has the family of light

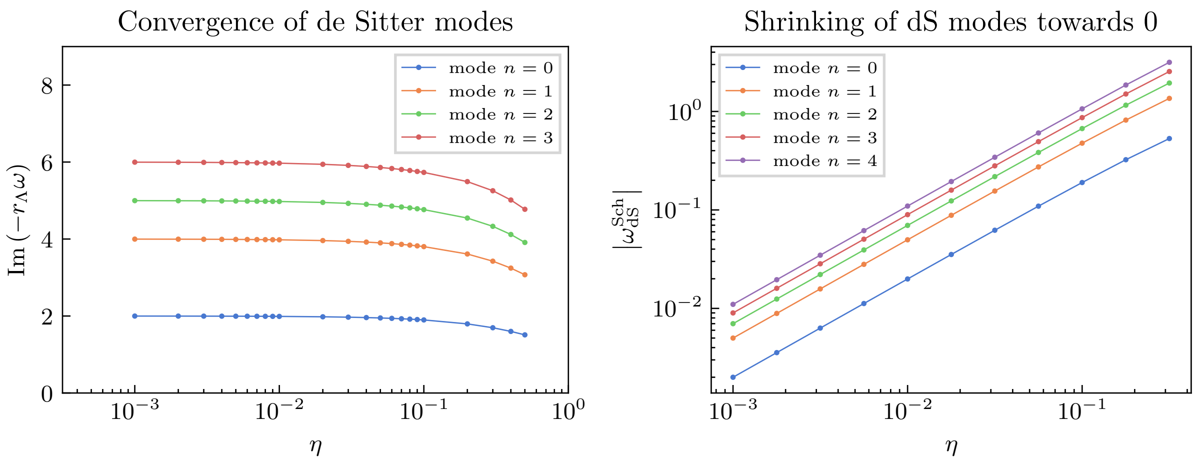

Figure 7: *Left Panel:* The convergence of de Sitter modes in de Sitter limiting scenario as $\eta \to 0$. The y-axis shows the absolute value of de Sitter modes with r_Λ as a typical length scale. The distance between the first overtone and the fundamental frequency is larger, while the distances between higher overtones show really good consistency. *Right Panel:* The equivalence of the left panel in Schwarzschild limiting scenario according to the relation in eq. (75). The de Sitter modes calculated in Schwarzschild limiting scenario $\omega^{\mathrm{Sch}}_{\mathrm{dS}}$ must shrink to 0 as $\mathcal{O}(\eta)$ when $\eta \to 0$. Thus, the equivalent values calculated within the de Sitter scenario $\omega^{\mathrm{dS}}_{\mathrm{dS}}$ remain finite.

ring modes and a branch cut at $\omega = 0$ up across the positive imaginary axes. This well known behaviour could be interpreted as a case of QNM instability, where a small deviation from pure Schwarzschild spacetime to Schwarzschild-de Sitter spacetime “breaks” the continuous spectra represented by the branch cut emerging from $\omega = 0$ along the positive imaginary axis into the dS modes as described above.

We could approach the instability phenomenon from the other way round. As $\eta \to 0$, we could observe an accumulation of the discrete QNMs near $\omega = 0$. Such accumulation could be quantified with the density of QNMs within a line segment $[a, b)$ along the imaginary axis

$$d(\eta; a, b) = \text{Num of QNMs}/(b - a). \tag{117}$$

Since the QNMs are discretely scattered along the imaginary axis, the density will not make sense if we put the line segment to be infinitely small. Instead, we track the region where the QNMs are evenly distributed on the imaginary axis. From Fig. 8 we could see that for any given η, the density of QNMs are consistent in the region of higher overtones. Therefore, it is natural to trace the density between certain overtone indices $\omega_{n=N}$ and $\omega_{n=N+M}$. Since Num of QNMs $= M$ in the line segment, and

$$\omega_{n=N}(\eta),\, \omega_{n=N+M}(\eta) \sim \mathcal{O}(\eta), \tag{118}$$

we find that the density associated with the region $\big[\omega_{n=N}(\eta),\, \omega_{n=N+M}(\eta)\big)$ explodes as η^{-1}. In the limit $\eta \to 0$, both ends of the line segment go to the origin $\omega = 0$, therefore we could expect a infinite density of QNMs at the origin in the limit, as is observed in Fig. 8.

As a conclusion, the numerical results show consistency between the two scenarios in such sense when $\eta \neq 0$. In the limit $\eta \to 0$, the results of the two scenarios go to each of the geometrical limit. The light ring modes in the Schwarzschild scenario $\omega^{\mathrm{Sch}}_{\mathrm{LR}}$ converges as $\eta \to 0$. Their limits are the corresponding modes in pure Schwarzschild spacetime. Therefore, the light ring modes in the de Sitter scenario $\omega^{\mathrm{dS}}_{\mathrm{LR}}$ must explode as η^{-1}, which is illustrated in Fig. 6. On the other hand, the de Sitter modes in the de Sitter scenario $\omega^{\mathrm{dS}}_{\mathrm{dS}}$ also converges to the corresponding modes in pure de Sitter spacetime when $\eta \to 0$. Therefore, these modes

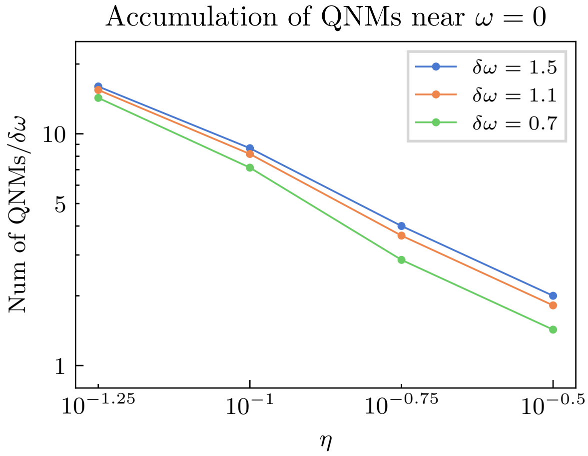

Figure 8: Behaviour of the de Sitter modes in the extremal limit $\eta \to 0$ when calculating within the Schwarzschild scenario. The accumulation of $\omega_{\rm dS}^{\rm Sch}$ near $\omega = 0$ is quantified by the density of QNMs within the line segment $\mathrm{Im}(\omega) \in (0, \delta\omega)$ as $\eta \to 0$. The density of QNMs being roughly consistent with a relatively larger $\delta\omega$ indicates an overall even distribution of $\omega_{\rm dS}^{\rm Sch}$ for higher overtones. The density of QNMs being proportional to η^{-1} could be inferred from the shrinking of $\omega_{\rm dS}^{\rm Sch}$ with η as shown in the top panel.

calculated in Schwarzschild scenario $\omega_{\rm dS}^{\rm Sch}$ must shrink to 0 as $\mathcal{O}(\eta)$, which is shown in the left panel of Fig. 8. We could interpret such a behaviour in the sense of the "density" of the QNMs on the imaginary axis increasing as $\eta \to 0$. This idea is examined by counting the number of QNMs within a certain line segment $\mathrm{Im}(\omega) \in (0, \delta\omega)$, which is shown in the right panel of Fig. 8. The numbers of QNMs turned out roughly proportional to $\delta\omega$ indicates an overall even distribution of $\omega_{\rm dS}^{\rm Sch}$, justifying our usage of the term "density". Therefore we could see the accumulation of QNMs near the origin $\omega = 0$, *i.e.* the density of $\omega_{\rm dS}^{\rm Sch}$ near the origin $\omega = 0$ increases as $\mathcal{O}(\eta^{-1})$ when $\eta \to 0$.

7.3 the extremal limit

As η approaches 1, the choice of the typical length scale r_H or r_Λ show no difference as $\omega^{\rm Sch} = \eta\omega^{\rm dS}, \quad \eta \to 1$. Instead we need to take into consideration the rescaling of the length scale $\lambda = r_H/\epsilon$ with $\epsilon = 1-\eta$. The results show that the light ring modes shrink proportionally (to the leading order) with regard to $\epsilon = 1 - \eta$ while the de Sitter modes shrink to a non-zero value as $\epsilon \to 0$, as illustrated in Fig. 9. Therefore the rescaled frequency $\omega^{\rm ExtLimit} = \omega^{\rm Sch}/\epsilon$ of the light ring modes converges but the de Sitter modes diverge to infinity, which recovers the results of the Nariai scenario as discussed in sec. 5.3. Comparing to the exact solutions provided by the theoretical analysis, our numerical strategy on this spacetime limit gives out results with superb accuracy. The fundamental mode is accurate up to 10^{-155} when the numerical precision is set to 10^{-160}, while the worse QNM are the higher overtones, where the error of overtone $n = 50$ decays to 10^{-28}.

Hence we have our full picture: the Schwarzschild-de Sitter spacetime have three distinct limits, the Schwarzschild limit, the de Sitter limit, and the Nariai limit. Moving from Schwarzschild spacetime to SdS spacetime, i.e. η increasing from 0 and r_H seen as the typical length scale, the de Sitter modes emerge from $r_H\omega = 0$ and take the position of the fundamental mode by definition, which is known as a type of "QNM instability". On the other hand, the light ring modes deviate smoothly from the pure Schwarzschild QNMs. If we instead start from de Sitter spacetime, i.e. η increasing from 0 and r_Λ seen as the typical length scale, the light ring modes show up from complex infinity, while the de Sitter modes deviate smoothly from the pure de Sitter modes. In such a scenario, the fundamental frequency is always the fundamental de Sitter mode. Nevertheless, the emergence of a new family of QNMs from the infinity could still be interpreted as a type of "QNM instability". The last spacetime limit is the Nariai limit, where η approaches 1 and the typical length scale is rescaled as r_H/ϵ. The light ring modes approaches the QNMs of the Nariai spacetime, which are known related to the PT potential, while the de Sitter modes diverge to infinity.

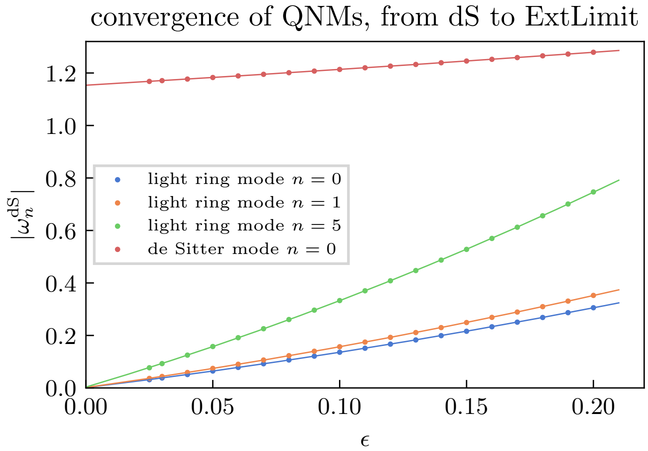

Figure 9: The convergence of $|\omega_{\mathrm{dS}}|$ as a function of $\epsilon = 1 - \eta$. Numerical error becomes prohibitive in extremal regions $\eta \approx 1$, so we use finite numerical results to fit the series expansion of $|\omega|(\epsilon)$. A fit in the form $|\omega| = a_0 + a_1\epsilon + a_2\epsilon^2$ gives $a_0 \neq 0$ for the de Sitter modes, specifically $a_0 = 1.15$ for mode $n = 0$ but the value depends on the overtone. For all the light ring modes $a_0 = 0$ indicates the linear relation $\omega_{\mathrm{LR}} \sim O(\epsilon)$.

8 Conclusion

Our work demonstrates a way of interpreting and understanding, from the QNM instability perspective, the new family of QNMs in Schwarzschild-de Sitter spacetime compared to Schwarzschild spacetime.

In our work we find that the perturbations on the background spacetime lead to both smooth deformations of existing QNMs and also the emergence of a new family of QNMs, the latter understood as a form of QNM instability. Specifically, in one way we consider the Schwarzschild scenario, where η the ratio of horizons r_H/r_Λ is a small perturbation acting on Schwarzschild spacetime. Then the light ring modes deform continuously and smoothly from their original values, while a new family of purely imaginary modes emerge from $r_H\omega = 0$ and destroy the branch cut. Equivalently if we approach the Schwarzschild limit from Schwarzschild-de Sitter spacetime, we find an accumulation with infinite density of these modes towards $r_H\omega = 0$, which corresponds to the branch cut structure in the limit to Schwarzschild spacetime. In another way we consider the de Sitter scenario, where η the ratio of horizons r_H/r_Λ is a small perturbation acting on de Sitter spacetime. Then the de Sitter modes deform smoothly while the light ring modes become the "unstable" family emerging from infinity. Finally with the Nariai scenario, $\epsilon = 1 - \eta$ is a small perturbation acting on Nariai spacetime. In such case the light ring modes deforms smoothly from the Pöschl-Teller modes, while the de Sitter modes are the "unstable" family emerging from infinity.

On the technical side, we employs the hyperboloidal framework and the Analytical Mesh Refinement technique to robustly solve the quasinormal mode problem. The hyperboloidal framework provides us with the ability to systematically and robustly control the geometries of the background spacetime to each spacetime limit. On top of this fundamental framework, we utilize the Analytical Mesh Refinement technique to improve our numerical capability of handling some extremely difficult situations. Together these technologies provide us with a working method of studying the QNMs under the geometrical limits of Schwarzschild-de Sitter spacetime.

Given the assumption of an asymptotically de Sitter background spacetime by current cosmological observations, what we find about the emergence of de Sitter modes under the Schwarzschild scenario could have implications in the time domain analysis of gravitational waves. One specific example is that it would affect the late-time tail evolution of gravitational waves, which might be possible for real-world detection. Besides, our robust geometrical framework to properly address spacetime limits can be extended to deal with complex spacetime solutions with more parameters, for example RN-de Sitter, or even Kerr-de Sitter and Kerr-Newman-de Sitter. Therefore it is possible for us to see a thorough interpretation of QNM instability for different QNM families of different background spacetimes.

References

[1] B. P. Abbott et al. Observation of Gravitational Waves from a Binary Black Hole Merger. *Phys. Rev. Lett.*, 116(6):061102, 2016.

[2] B. P. Abbott et al. GWTC-1: A Gravitational-Wave Transient Catalog of Compact Binary Mergers Observed by LIGO and Virgo during the First and Second Observing Runs. *Phys. Rev. X*, 9(3):031040, 2019.

[3] R. Abbott et al. GWTC-3: Compact Binary Coalescences Observed by LIGO and Virgo during the Second Part of the Third Observing Run. *Phys. Rev. X*, 13(4):041039, 2023.

[4] A. G. Abac et al. Observation of Gravitational Waves from the Coalescence of a 2.5–4.5 $M_\odot$ Compact Object and a Neutron Star. *Astrophys. J. Lett.*, 970(2):L34, 2024.

[5] R. Abbott et al. Tests of general relativity with binary black holes from the second LIGO-Virgo gravitational-wave transient catalog. *Phys. Rev. D*, 103(12):122002, 2021.

[6] R. Abbott et al. Tests of General Relativity with GWTC-3. 12 2021.

[7] Kostas D. Kokkotas and Bernd G. Schmidt. Quasinormal modes of stars and black holes. *Living Rev. Rel.*, 2:2, 1999.

[8] Hans-Peter Nollert. TOPICAL REVIEW: Quasinormal modes: the characteristic 'sound' of black holes and neutron stars. *Class. Quant. Grav.*, 16:R159–R216, 1999.

[9] Emanuele Berti, Vitor Cardoso, and Andrei O. Starinets. Quasinormal modes of black holes and black branes. *Class. Quant. Grav.*, 26:163001, 2009.

[10] R. A. Konoplya and A. Zhidenko. Quasinormal modes of black holes: From astrophysics to string theory. *Rev. Mod. Phys.*, 83:793–836, 2011.

[11] A. Lopez-Ortega. Quasinormal modes of D-dimensional de Sitter spacetime. *Gen. Rel. Grav.*, 38:1565–1591, 2006.

[12] Aron Jansen. Overdamped modes in Schwarzschild-de Sitter and a Mathematica package for the numerical computation of quasinormal modes. *Eur. Phys. J. Plus*, 132(12):546, 2017.

[13] Vitor Cardoso, João L. Costa, Kyriakos Destounis, Peter Hintz, and Aron Jansen. Quasinormal modes and Strong Cosmic Censorship. *Phys. Rev. Lett.*, 120(3):031103, 2018.

[14] Patrick R. Brady, Chris M. Chambers, William Krivan, and Pablo Laguna. Telling tails in the presence of a cosmological constant. *Phys. Rev. D*, 55:7538–7545, 1997.

[15] Gregorio Carullo and Marina De Amicis. Late-time tails in nonlinear evolutions of merging black hole binaries. 10 2023.

[16] Vitor Cardoso, Gregorio Carullo, Marina De Amicis, Francisco Duque, Takuya Katagiri, David Pereniguez, Jaime Redondo-Yuste, Thomas F. M. Spieksma, and Zhen Zhong. Hushing black holes: Tails in dynamical spacetimes. *Phys. Rev. D*, 109(12):L121502, 2024.

[17] Marina De Amicis, Simone Albanesi, and Gregorio Carullo. Inspiral-inherited ringdown tails. *Phys. Rev. D*, 110(10):104005, 2024.

[18] Mateus Malato Corrêa, Caio F. B. Macedo, and João Luís Rosa. Quasibound state reminiscent in de Sitter black holes: Quasinormal modes and the decay of massive fields. *Phys. Rev. D*, 109(8):084018, 2024.

[19] Peter Hintz and Andras Vasy. Semilinear wave equations on asymptotically de Sitter, Kerr–de Sitter and Minkowski spacetimes. *Anal. Part. Diff. Eq.*, 8(8):1807–1890, 2015.

[20] Peter Hintz and Andras Vasy. Global analysis of quasilinear wave equations on asymptotically Kerr-de Sitter spaces. *Int. Math. Res. Not.*, 2016(17):5355–5426, 2016.

[21] Peter Hintz and András Vasy. The global non-linear stability of the Kerr-de Sitter family of black holes. 6 2016.

[22] R. A. Konoplya and A. Zhidenko. Nonoscillatory gravitational quasinormal modes and telling tails for Schwarzschild–de Sitter black holes. *Phys. Rev. D*, 106(12):124004, 2022.

[23] Sean Fortuna and Ian Vega. Bernstein spectral method for quasinormal modes and other eigenvalue problems. *Eur. Phys. J. C*, 83(12):1170, 2023.

[24] Anil Zenginoglu. A Geometric framework for black hole perturbations. *Phys. Rev. D*, 83:127502, 2011.

[25] Rodrigo Panosso Macedo. Hyperboloidal approach for static spherically symmetric spacetimes: a didactical introduction and applications in black-hole physics. *Phil. Trans. Roy. Soc. Lond. A*, 382:20230046, 2024.

[26] Rodrigo Panosso Macedo and Anil Zenginoglu. Hyperboloidal approach to quasinormal modes. *Front. in Phys.*, 12:1497601, 2024.

[27] Subhodeep Sarkar, Mostafizur Rahman, and Sumanta Chakraborty. Perturbing the perturbed: Stability of quasinormal modes in presence of a positive cosmological constant. *Phys. Rev. D*, 108(10):104002, 2023.

[28] Kyriakos Destounis, Valentin Boyanov, and Rodrigo Panosso Macedo. Pseudospectrum of de Sitter black holes. *Phys. Rev. D*, 109(4):044023, 2024.

[29] Vitor Cardoso, Shilpa Kastha, and Rodrigo Panosso Macedo. Physical significance of the black hole quasinormal mode spectra instability. *Phys. Rev. D*, 110(2):024016, 2024.

[30] Robert P. Geroch. Limits of spacetimes. *Commun. Math. Phys.*, 13:180–193, 1969.

[31] Reinhard Meinel, Marcus Ansorg, Andreas Kleinwachter, Gernot Neugebauer, and David Petroff. *Relativistic Figures of Equilibrium.* Cambridge University Press, Cambridge, UK, 2008.

[32] Yu-Chun Pynn, Rodrigo Panosso Macedo, Martin Breithaupt, Stefan Palenta, and Reinhard Meinel. Gyromagnetic factor of rotating disks of electrically charged dust in general relativity. *Phys. Rev. D*, 94(10):104035, 2016.

[33] Rodrigo Panosso Macedo, Benjamin Leather, Niels Warburton, Barry Wardell, and Anıl Zenginoğlu. Hyperboloidal method for frequency-domain self-force calculations. *Phys. Rev. D*, 105(10):104033, 2022.

[34] José Luis Jaramillo, Rodrigo Panosso Macedo, and Lamis Al Sheikh. Pseudospectrum and Black Hole Quasinormal Mode Instability. *Phys. Rev. X*, 11(3):031003, 2021.

[35] Sean M. Carroll, Matthew C. Johnson, and Lisa Randall. Extremal limits and black hole entropy. *JHEP*, 11:109, 2009.

[36] Marc Casals, Sam R. Dolan, Adrian C. Ottewill, and Barry Wardell. Self-Force Calculations with Matched Expansions and Quasinormal Mode Sums. *Phys. Rev. D*, 79:124043, 2009.